

# Water Resources Research®

## RESEARCH ARTICLE

10.1029/2022WR034293

### Key Points:

- Poroelastic response is governed by an interconnection between aquifer hydraulic diffusivity, Biot-Willis coefficient, and elastic moduli
- Small tilt arrays can potentially provide information on relative conduit location and size
- Heterogeneity, complex geometry, and non-uniqueness present challenges in progressing from synthetic simulations to real-world predictions

### Supporting Information:

Supporting Information may be found in the online version of this article.

### Correspondence to:

J. A. Gochenour,  
[gochenja@nv.doe.gov](mailto:gochenja@nv.doe.gov)

### Citation:

Gochenour, J. A., Rinehart, A. J., Luhmann, A. J., Grapenthin, R., & Bilek, S. L. (2024). Poroelastic response to karst conduit pressurization: A finite element modeling exercise toward the use of tiltmeters in karst aquifer monitoring applications. *Water Resources Research*, 60, e2022WR034293. <https://doi.org/10.1029/2022WR034293>

Received 9 DEC 2022

Accepted 5 JUN 2024

© 2024. The Authors.

This is an open access article under the terms of the [Creative Commons Attribution-NonCommercial-NoDerivs License](#), which permits use and distribution in any medium, provided the original work is properly cited, the use is non-commercial and no modifications or adaptations are made.

## Poroelastic Response to Karst Conduit Pressurization: A Finite Element Modeling Exercise Toward the Use of Tiltmeters in Karst Aquifer Monitoring Applications

Jacob Alexander Gochenour<sup>1</sup> , Alex J. Rinehart<sup>1</sup> , Andrew J. Luhmann<sup>2</sup> , Ronni Grapenthin<sup>3</sup> , and Susan L. Bilek<sup>1</sup> 

<sup>1</sup>New Mexico Institute of Mining and Technology, Earth and Environmental Science, Socorro, NM, USA, <sup>2</sup>Wheaton College, Earth and Environmental Science, Wheaton, IL, USA, <sup>3</sup>Department Geosciences, Geophysical Institute, University of Alaska Fairbanks, Fairbanks, AK, USA

**Abstract** Tiltmeters have the potential to resolve ground deformation due to changes in hydraulic head induced by conduit pressurization. Conduit pressure variations cause groundwater to be stored or released from storage within the surrounding rock matrix. We modeled this process and infer whether the resulting deformation is measurable with tiltmeters and what behavior to expect by fully coupling porous media flow and solid mechanics in a poroelastic, 2D finite element model. Parameter sets globally representative of Paleozoic, Mesozoic, and Cenozoic confined and unconfined aquifers are considered. Our analysis focuses on the impact of the parameterization on pore pressure, vertical displacement, and tilt. We find that the spatial distribution of the poroelastic signal depends on the hydraulic diffusivity, and its magnitude depends on the mechanical and coupling parameters. Additional analysis of the impacts of conduit radius and depth suggests that tilt polarity could be an indicator of conduit location and relative conduit size. We calibrated the model to data observations acquired at the Santa Fe River Sink-Rise system in north-central Florida, US. We find that an overlying clay-rich layer may act to partially confine the aquifer. Although the observed tilt signal is present in radial and transverse components and polarity reversals occur, we were able to recover the magnitude and general trend of the tilt response.

**Plain Language Summary** Our study focused on understanding how changes in ground deformation can be caused by groundwater flow induced by a pressurized karst conduit. We modeled this process in different types of aquifers to determine if the deformation can be measured using tiltmeters, instruments that measure changes in the angle of the ground. We also explored the effect of conduit size and depth. Our findings show that the distribution and magnitude of the ground response depend on the physical parameters of the aquifer. Additionally, we find that tilt data can provide information about conduit location, size, and depth. We tested the model using data from the Santa Fe River Sink-Rise system in Florida. We find this system may behave as a partially confined aquifer due to the presence of clay in the overlying unit. From the use of our simplified numerical formulation, we were able to recover the magnitude and overall trend of the observed tilt data.

## 1. Introduction

Erosional features formed due to the dissolution of soluble rock define karst landscapes (Veress, 2020) and can generate incredibly complex hydrological properties in the resulting rocks (Ford & Williams, 2007). Namely, dissolutionally enlarged channels or conduits play a central role in these systems, accounting for most groundwater flow, which is highly localized and challenging to detect (Budd & Vacher, 2004). However, groundwater storage and pumping predominantly occur within the surrounding porous rock matrix (Worthington et al., 2000). Exchange between conduits and the rock matrix controls water quality because conduits may provide direct and rapid access to groundwater for contaminants (Vesper et al., 2000; White, 2002).

Despite the significance of understanding conduit-matrix interactions, the local heterogeneity of the conduits and porous media aquifer poses challenges in identifying the conduit's location and characterizing the aquifer's hydrological parameters. Various techniques, including hydrological (e.g., Bailly-Comte et al., 2010; Covington et al., 2009; J. M. Martin et al., 2006), geochemical (e.g., Birk et al., 2006; Gunn, 2015; J. B. Martin & Dean, 1999, 2001; Moore et al., 2009, 2010; Sreaton et al., 2004), numerical modeling-based (e.g., Basha & Zoghbi, 2018; Hubinger et al., 2016; Wilson & Henry, 2014; Zhang et al., 2022), and geophysical methods (e.g.,

Bechtel et al., 2007; Benson et al., 2003; Chalikakis et al., 2011) have been adopted to address this challenge; however, combining geodetic techniques and numerical modeling is a relatively nascent approach.

Geodetic techniques have been used extensively in studying volcanism-induced ground deformation, encompassing phenomena like dike intrusions, fracture propagation, lava fountains, and pressurization within magmatic or hydrothermal systems that lead to volumetric changes in the volcanic structure (Fernández et al., 2017; Gambino et al., 2014). However, these techniques can also provide observations of deformation induced by groundwater pressurized sources, such as faults (e.g., Devoti et al., 2018; Schuite et al., 2017), pumping or injecting wells (e.g., Fabian & Kümpel, 2003; Hisz et al., 2013; Kümpel et al., 1996, 1999; Murdoch et al., 2021, 2023; Weise et al., 1999), fractures (e.g., D'Agostino et al., 2018; Hisz et al., 2013; Jacob et al., 2010; Lesparre et al., 2017; Longuevergne et al., 2009; Pintori et al., 2021; Serpelloni et al., 2018; Silverii et al., 2016, 2019), and conduits (e.g., Braitenberg et al., 2019). Tiltmeters are especially useful for studying these phenomena. Because heterogeneities affect flow patterns through aquifer systems, they also manifest in the temporal aspects, orientation, and extent of the tilt (Fabian & Kümpel, 2003; Hisz et al., 2013; Lesparre et al., 2017). Therefore, tiltmeters can provide clues on the type, location, and geometry of aquifer heterogeneities, enhancing our knowledge of the aquifer structure and behavior.

Understanding the role of the pressurized sources, as monitored by geodetic techniques, is necessary for comprehending heterogeneous aquifer system dynamics. As governed by the theory of poroelasticity (Biot, 1941, 1962; Biot & Willis, 1957), the direct coupling between hydraulic pressure transients and porous media deformation can offer details on aquifer state, properties, and boundary conditions (Fabian & Kümpel, 2003; Weise et al., 1999). Some studies have partially addressed geodetics and poroelasticity through numerical modeling of the pressure source while neglecting flow through the porous matrix (e.g., Braitenberg et al., 2019; Jacob et al., 2010; Longuevergne et al., 2009). Although, other studies have considered fully coupled poroelastic models (e.g., Hisz et al., 2013; Murdoch et al., 2021, 2023; Schuite et al., 2017; Tsai, 2011; Weise et al., 1999).

This paper explores the poroelastic response to karst conduit pressurization in an idealized 2D cross-sectional finite element model implemented in COMSOL Multiphysics® (v. 6.0) (COMSOL, 2021). Because hydrologic and mechanical parameters may differ by large amounts between aquifer types and age, the poroelastic response, given a simple linear input, is compared between geometrically similar Paleozoic, Mesozoic, and Cenozoic age confined and unconfined aquifers. That is, we chose parameter sets to globally represent aquifer types through progressively older to younger limestone, which have typically experienced deeper to shallower burial and define tectonic and eogenetic karst (Choquette & Pray, 1970; Florea & Vacher, 2006; Vacher & Mylroie, 2002). For example, matrix permeability and aquifer age generally have an exponential relationship, and the permeability of the two endmember groups of carbonate rocks can differ by more than seven orders of magnitude (Florea & Vacher, 2006). The effects of conduit size and depth are further explored in a Cenozoic unconfined aquifer case. Finally, the Cenozoic unconfined aquifer model is roughly calibrated and compared to hydrologic and tilt observations made between July 2019 and October 2019 at the Santa Fe River Sink-Rise System (SRS) in north-central Florida, US.

## 2. Linear Poroelastic Constitutive Relationships

The constitutive relationships of poroelasticity were originally developed in Biot (1941), Biot and Willis (1957), and Biot (1962), assuming reversible stress-strain relations given small strains and porous media flow follows Darcy's law. Detournay and Cheng (1993) and Wang (2000) provide additional details on the theory of linear poroelasticity. We present these relations considering additional simplifying assumptions such as that the medium is hydrologically isotropic and gravity is negligible (Text S1, Table S1, & Figures S1 and S2 in Supporting Information S1). The relations fully couple porous media flow to solid mechanics, and we simultaneously solve for displacement and fluid pressure via finite element analysis in COMSOL Multiphysics® (v. 6.0), by coupling the Subsurface Flow and Solid Mechanics modules.

Biot (1962) introduced the second-order symmetrical total stress tensor,  $\tau_{ij}$ , that describes the forces applied to both solid and fluid parts of each face of a unit cube and can be expressed as

$$\tau_{ij} = 2\mu\epsilon_{ij} + \lambda\epsilon_{\text{vol}}\delta_{ij} - \alpha p\delta_{ij} \quad (1)$$

**Table 1**  
*List of Symbols Introduced*

$b$	Aquifer saturated thickness [L]	$x$	Horizontal Cartesian coordinate [L]
$D$	Conduit depth [L]	$y$	Vertical Cartesian coordinate [L]
$E$	Drained Young's modulus [F/L <sup>2</sup> ]	$\alpha$	Biot-Willis coefficient [1]
$g$	Acceleration due to gravity, scalar [L/T <sup>2</sup> ]	$\gamma$	Fluid specific weight [F/L <sup>3</sup> ]
$i$	Cartesian coordinate index	$\delta_{ij}$	Kronecker delta [1]
$j$	Cartesian coordinate index	$\epsilon_{ij}$	Small strain tensor [1]
$K_d$	Drained bulk modulus [F/L <sup>2</sup> ]	$\epsilon_{vol}$	Volumetric strain (i.e., dilatation) [1]
$k$	Isotropic permeability [L <sup>2</sup> ]	$\eta$	Dynamic viscosity [FT/L <sup>2</sup> ]
$n$	Matrix porosity [1]	$\theta$	Tilt [1] or [nrad]
$p$	Fluid pressure [F/L <sup>2</sup> ]	$\kappa$	Aquifer hydraulic diffusivity [L <sup>2</sup> /T]
$R$	Conduit radius [L]	$\lambda$	Lamé parameter [F/L <sup>2</sup> ]
$S$	Specific storage coefficient [L <sup>2</sup> /F]	$\rho_f$	Fluid density [M/L <sup>3</sup> ]
$S_s$	Specific storage [L <sup>-1</sup> ]	$\tau_{ij}$	Total stress tensor [F/L <sup>2</sup> ]
$S_y$	Specific yield [1]	$\tau_{ij,j}$	Divergence of total stress tensor [F/L <sup>3</sup> ]
$t$	Time [T]	$\mu$	Shear modulus [F/L <sup>2</sup> ]
$u$	Horizontal displacement component [L]	$\nu$	Drained Poisson's ratio [1]
$v$	Vertical displacement component [L]	$\chi_f$	Fluid compressibility [L <sup>2</sup> /F]
$w_x$	Far-field boundary [L]		

where  $\mu$  is the shear modulus,  $\lambda$  is the drained Lamé constant,  $\alpha$  is the Biot-Willis coefficient (Biot & Willis, 1957),  $\epsilon_{ij}$  is the small strain tensor,  $\epsilon_{vol}$  is the volumetric strain,  $p$  is the fluid pressure, and  $\delta_{ij}$  is the Kronecker delta (Table 1). The shear modulus and drained Lamé constant are related to drained Young's modulus,  $E$ , and drained Poisson's ratio,  $\nu$ , by  $\mu = E/[2(1 + \nu)]$  and  $\lambda = \nu E/[(1 + \nu)(1 - 2\nu)]$ , respectively. Strain is considered to be positive in expansion and negative in compression. It is assumed that the total stress field is in equilibrium, that is, when gravity is neglected,

$$\tau_{ij,j} = 0 \quad (2)$$

where  $\tau_{ij,j}$  is the divergence of the second-order stress tensor. The fluid is considered to be at rest and under constant pressure.

For a hydrologically isotropic medium and when gravity is neglected, fluid flow in a poroelastic medium is governed by (e.g., Bear, 1972, 1979; Detournay & Cheng, 1993; Wang, 2000)

$$S \frac{\partial p}{\partial t} - \frac{k}{\eta} \nabla^2 p = -\alpha \frac{\partial \epsilon_{vol}}{\partial t} \quad (3)$$

where  $S$  is the specific storage coefficient,  $k$  is permeability, and  $\eta$  is the dynamic viscosity of the fluid. The mass source-sink coupling term,  $-\alpha \partial \epsilon_{vol} / \partial t$ , describes the rate of expansion or contraction of pore space. Because we are interested in transient processes, we can neglect gravity by assuming that the groundwater has negligible variations in density (Anderson et al., 2015; Wang, 2000). Nonetheless, we showed that simulations with gravity do not significantly change the results compared to pressure-only simulations, but are much more computationally expensive (Text S1, Table S1, & Figures S1 and S2 in Supporting Information S1). These simulations show that the pressure gradients within the aquifer, induced from the localized fluid injection and withdrawal within the conduit, are the dominant drivers of the system dynamics. Additionally, these simulations suggest that gravitational consolidation of the solid skeleton is also negligible. Consequently, the effect of gravity on the observed transients is minimal and does not influence interpretations of results.

Although Equation 3 is time-varying, Equation 2 is quasi-static. It is assumed that an elastic response of the solid to changes in fluid flow results in instantaneous transitions to a new equilibrium state (Bear, 1972). This assumption may be violated for granular unconsolidated materials and cohesive soils (i.e., sand and clay) because both behave inelastically and involve more time for the stress state to reach a new equilibrium (Bear, 1972).

Biot and Willis (1957) used jacketed and unjacketed compressibility tests after Hughes and Cooke (1953) and Geertsma (1956) to measure the Biot-Willis coefficient and the storage coefficient in terms of solid and fluid compressibility. They show that

$$S = n\chi_f + \frac{(\alpha - n)(1 - \alpha)}{K_d} \quad (4)$$

where  $\chi_f$  is the fluid compressibility,  $n$  is porosity, and  $K_d$  is the drained bulk modulus, related to shear modulus and drained Lamé constant by  $K_d = \frac{2}{3}\mu + \lambda$ .

Equation 3 describes the flow in confined aquifers; however, we assume the changes in the hydraulic head are negligible in the unconfined simulations and adopt a fixed-node approach as typically used in MODFLOW (Anderson et al., 2015; Sheets et al., 2015). Although COMSOL<sup>®</sup> (v. 6.0) does not offer explicit definition of specific yield,  $S_y$ , for an unconfined aquifer, it can be added to the fluid compressibility input within the poroelastic storage node as

$$\chi_f \rightarrow \chi_f + \frac{S_y}{n\rho_f g b} \quad (5)$$

where  $\rho_f$  is the fluid density,  $b$  is the initial aquifer saturated thickness, and  $g$  is acceleration due to gravity. Simulating unconfined aquifer pump tests in COMSOL<sup>®</sup> by defining  $\chi_f$  in this manner agrees with analytical solutions of the Theis (1935) well drawdown equation for given values of  $S_y$  (Text S2, Table S2, & Figure S3 in Supporting Information S1).

Given boundary and initial conditions, the final formulation can be found by substituting Equation 1 into Equation 2, and substituting Equations 4 and 5 into Equation 3. This can then be solved for displacements,  $u$  and  $v$ , and fluid pressure  $p$ . Because tiltmeters generally measure changes from vertical level, the tilt,  $\theta$ , is calculated as the gradient of the vertical displacement field,  $v$  (i.e.,  $\theta = \text{atan}(\partial v / \partial x)$ , for 2D).

Since we model confined and unconfined aquifers, we need to consider the respective large differences in hydraulic diffusivity,  $\kappa$ , as this parameter governs the speed with which pressure disturbances will propagate through the aquifer. Hydraulic diffusivity can be defined in terms of permeability and specific storage,  $S_s$ , as

$$\kappa = \frac{k\rho_f g}{\eta S_s} \quad (6)$$

For poroelastic considerations,  $S_s$  can be obtained by combining Equations 4 and 5, and then factoring in the specific weight of the fluid,  $\gamma = \rho_f g$ . Thus, by using the relationships between elastic moduli, Equation 6 can be expressed as

$$\kappa = \frac{k}{\eta \left( n\chi_f + 3(\alpha - n)(1 - \alpha)(1 - 2\nu)E^{-1} + S_y b^{-1} \gamma^{-1} \right)} \quad (7)$$

### 3. Model Formulation

#### 3.1. Geometry, Parameters, Boundary, and Initial Conditions

To understand the general poroelastic response to karst conduit pressurization and subsequent change in groundwater storage, we developed an idealized two-dimensional cross-sectional model geometry in COMSOL Multiphysics<sup>®</sup> (v. 6.0). A semicircle, representing a cross-sectional area across the half-width of a cylindrical karst conduit, was centrally embedded along a plane of symmetry (mirror symmetry along the  $xy$ -plane) within a

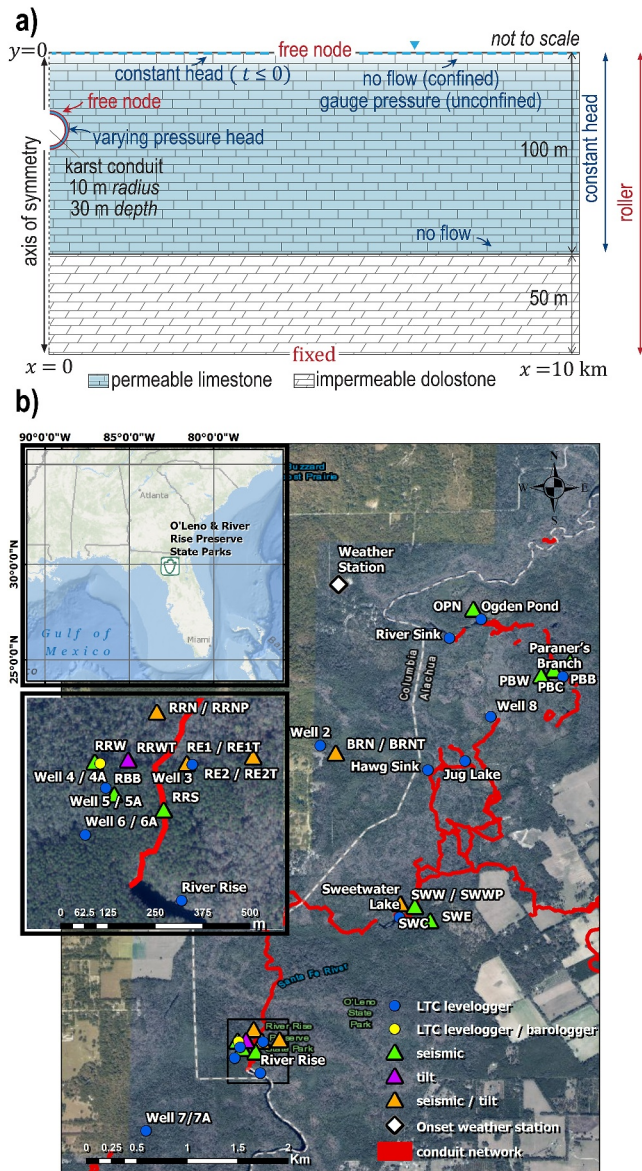


**Figure 1.** (a) Model geometry with boundary and initial conditions. (b) Map depicting the Santa Fe River Sink-Rise (SRS) system and instrumentation deployment from May 2018–May 2021. Map sourced from Esri contributors, and conduit overlay provided by the Santa Fe River Rise Project of the National Speleological Society Cave Diving Section, contact [mpoucher@cavesurvey.com](mailto:mpoucher@cavesurvey.com).

horizontally stratified aquifer of constant thickness (Figure 1a). Model strata consisted of an impermeable lower-confining dolostone unit and a fully saturated permeable limestone unit. These were based on the Upper Floridan Aquifer (UFA) of north-central Florida between the cities of Gainesville and Lake City (Florida Geological Survey, 1997; Miller, 1986, 1990; Upchurch et al., 2019; Williams & Kuniansky, 2016). The conduit, located within the permeable zone, embodied a local part of the UFA known as the Santa Fe River Sink-Rise System (SRS), a land bridge overlying a network of karst conduits that connect the northern and southern branches of the Santa Fe River (Upchurch et al., 2019) (Figure 1b). The fully submerged conduits, mapped by the National Speleological Society Cave Diving Section's Santa Fe River Rise Project (Courbon et al., 2005), measure approximately 18–24 m in width and 12–18 m in height and are 30 m beneath the surface (Moore et al., 2010; Sreaton et al., 2004). The UFA is considered to be unconfined here and consists of Eocene age permeable limestone (Ocala formation) (Williams & Kuniansky, 2016). Its uppermost unit of post-Miocene undifferentiated sand and clay (Florida Geological Survey, 1997; Miller, 1986; Ritorto et al., 2009; Upchurch et al., 2019; Williams & Kuniansky, 2016) was neglected in the initial aquifer case studies to allow comparison between confined and unconfined aquifer cases of coherent initial saturated thickness. However, we tested the potential effect of the uppermost unit when incorporating natural data observations at the SRS into the model.

All parameter values used in this study are presented in Table 2. These represent case studies of the model permeable zone ranging from Paleozoic limestone to Cenozoic limestone (e.g., Budd & Vacher, 2004; Choquette & Pray, 1970; J. M. Martin et al., 2006; Vacher & Mylroie, 2002). Values for the lower confining unit were held constant.

We assumed a plane of symmetry at  $x = 0$ . This forced a condition of zero solid displacement and fluid flow normal to  $x = 0$  but allowed vertical ( $y$ -plane) groundwater flow and deformation at the  $x = 0$  boundary (Figure 1a). The far-field boundary was located at  $x = w_x$ . Mechanical roller boundaries were applied at the far-field boundary for all domains that also forced a condition of zero solid displacement normal to the boundary. Constant hydraulic head conditions were applied to the permeable zone far-field boundary such that fluid was allowed to flow in or beyond the boundary. In the confined case, the permeable zone was confined top and bottom with no-flow boundaries in which flow could not occur in a direction across the boundary. For the unconfined case, the permeable zone was confined at the bottom with a no-flow boundary, while a gauge pressure condition was placed on the upper boundary. The lower boundary on the lower confining unit was mechanically fixed and could not experience deformation. Mechanical free node conditions were applied to the uppermost and conduit boundaries; thus, the land surface and conduit walls were free to deform.

For the aquifer domain, an initial hydraulic head condition was set to a uniform pressure head and zero elevation head at the boundary between the permeable zone and the upper confining unit (at  $y = 0$  for  $t \leq 0$ ). We defined a fluid boundary condition at the conduit-matrix edge by assuming that the conduit pressure head was equivalent to the matrix hydraulic head at the boundary (Basha & Zoghbi, 2018), which applied a fluid pressure gradient,  $\nabla p$ , on Equation 3 that induced flow.

The SRS features approximately north-south oriented conduits (Figure 1b), which are situated between the Florida coastlines where the width of the UFA extends  $\sim 200$  km from east to west (Upchurch et al., 2019; Williams & Kuniansky, 2016). This suggests that model far-field boundaries should be located approximately  $\pm 100$  km from the conduit center. To gauge if this distance can be decreased, thus allowing for smaller model

**Table 2**  
*Parameter Sets for Comparison Between Different Limestone Age and Aquifer Type*

Parameter	Symbol	Paleozoic	Mesozoic	Cenozoic	Dimension
Aquifer porosity <sup>a</sup>	$n$	0.02	0.10	0.20	[1]
Aquifer permeability <sup>a</sup>	$k$	$10^{-17}$	$10^{-15}$	$10^{-13}$	[m <sup>2</sup> ]
Aquifer specific yield <sup>b</sup>	$S_y$	0.015	0.075	0.150	[1]
Aquifer Biot coefficient <sup>c</sup>	$\alpha$	0.10	0.40	0.65	[1]
Limestone Young's modulus <sup>d</sup>	$E$	52	35	23	[GPa]
Limestone Poisson's ratio <sup>c</sup>	$\nu$	0.25	0.30	0.35	[1]
Dolostone Young's modulus <sup>e,f</sup>	$E$		57.8		[GPa]
Dolostone Poisson's ratio <sup>e,f</sup>	$\nu$		0.225		[1]
Water density <sup>g,f</sup>	$\rho_f$		1000		[kg/m <sup>3</sup> ]
Water compressibility <sup>g,f</sup>	$\chi_f$		$4.4 \cdot 10^{-10}$		[Pa <sup>-1</sup> ]
Water dynamic viscosity (21°C) <sup>h,f</sup>	$\eta$		0.9779		[cP]
Confined hydraulic diffusivity <sup>i</sup>	$\kappa$	$9.40 \cdot 10^{-4}$	$2.04 \cdot 10^{-2}$	$1.09 \cdot 10^0$	[m <sup>2</sup> /s]
Unconfined hydraulic diffusivity <sup>i</sup>	$\kappa$	$6.68 \cdot 10^{-7}$	$1.34 \cdot 10^{-5}$	$6.68 \cdot 10^{-4}$	[m <sup>2</sup> /s]

<sup>a</sup>Values typical of limestone age (e.g., Budd & Vacher, 2004; Ford & Williams, 2007; Martin et al., 2006; Vacher & Mylroie, 2002). <sup>b</sup>Value for unconfined cases assumed to be 75% of porosity. <sup>c</sup>Values as a function of matrix porosity (T. Bratton, Personal Commun., March 2021). <sup>d</sup>Static values for limestone as a function of porosity after Hadi (2018). <sup>e</sup>Typical value ranges from Appendices D and E of Gudmundsson (2011) under the assumption of decreasing Poisson's ratio with porosity (e.g., Diaz et al., 2003; Fabricius et al., 2007; Ji et al., 2018). <sup>g</sup>Typical value from Freeze and Cherry (1979). <sup>h</sup>Values from Weast et al. (1992). <sup>i</sup>Values calculated from Equation 7 assuming zero specific yield for the confined cases. <sup>f</sup>Value used across all study cases.

elements as opposed to a coarser mesh, the far-field boundary was refined such that three separate models with  $w_x < 100$  km were compared to a reference model with  $w_x = 100$  km. This analysis suggests that  $w_x$  for this study should be no more than 10 km from the conduit center (Text S3, Table S3, & Figures S4 and S5 in Supporting Information S1). Analysis of the behavior of the poroelastic signal, while considering the location of geophysical and hydrological instrumentation deployed at the SRS (Figure 1b), suggests that the region of interest within the model falls within 250 m of the conduit. We conducted a mesh resolution study within the region of interest, refining the mesh element size until the solutions converged to constant values (Text S4, Table S4, & Figures S6–S8 in Supporting Information S1).

### 3.2. Aquifer Cases

This study explored the effects of different parameter sets and modifications to conduit geometry. We considered parameter sets representative of Paleozoic, Mesozoic, and Cenozoic limestone (Table 2) for both confined and unconfined aquifer cases. Additionally, we considered confined and unconfined Cenozoic limestone cases, and conduit radius,  $R$ , and depth to the conduit center,  $D$ , are tested over the following sets: (a) radii of 1, 5, 10, and 15 m at a depth of 30 m and (b) radius of 10 m at depths of 15, 30, 45, and 60 m. Although conduit processes can occur at time scales as low as fractions of a second, driven by pressure waves propagating at the speed of sound, we are interested in matrix responses to long-term changes in conduit pressure over days to months. For all tests, the conduit pressure head was assigned to increase at a rate of 0.5 cm/hr with a time-step of 0.25 days over 25 days. This corresponds to the average rate of groundwater and surface-water level increase observed in hydrograph rising limbs from SRS monitoring locations and represents a reasonable duration for a complete SRS rising limb (Figure S4 in Supporting Information S1). Displacement and tilt results are compared first at a fixed time and  $y$ -position ( $t = 25$  days and  $y = 0$ ), and then at a fixed  $y$ -position and  $x$ -position ( $y = 0$  and  $x = 15, 45, 70,$  and  $175$  m) from the conduit center, where all the fixed  $xy$ -positions, except  $x = 1$  m, correspond to conduit-tiltmeter distance at the study site (Figure 1b). The hydraulic head results are compared at similar positions, except roughly at the depth of the monitoring wells ( $y = -30$  m).

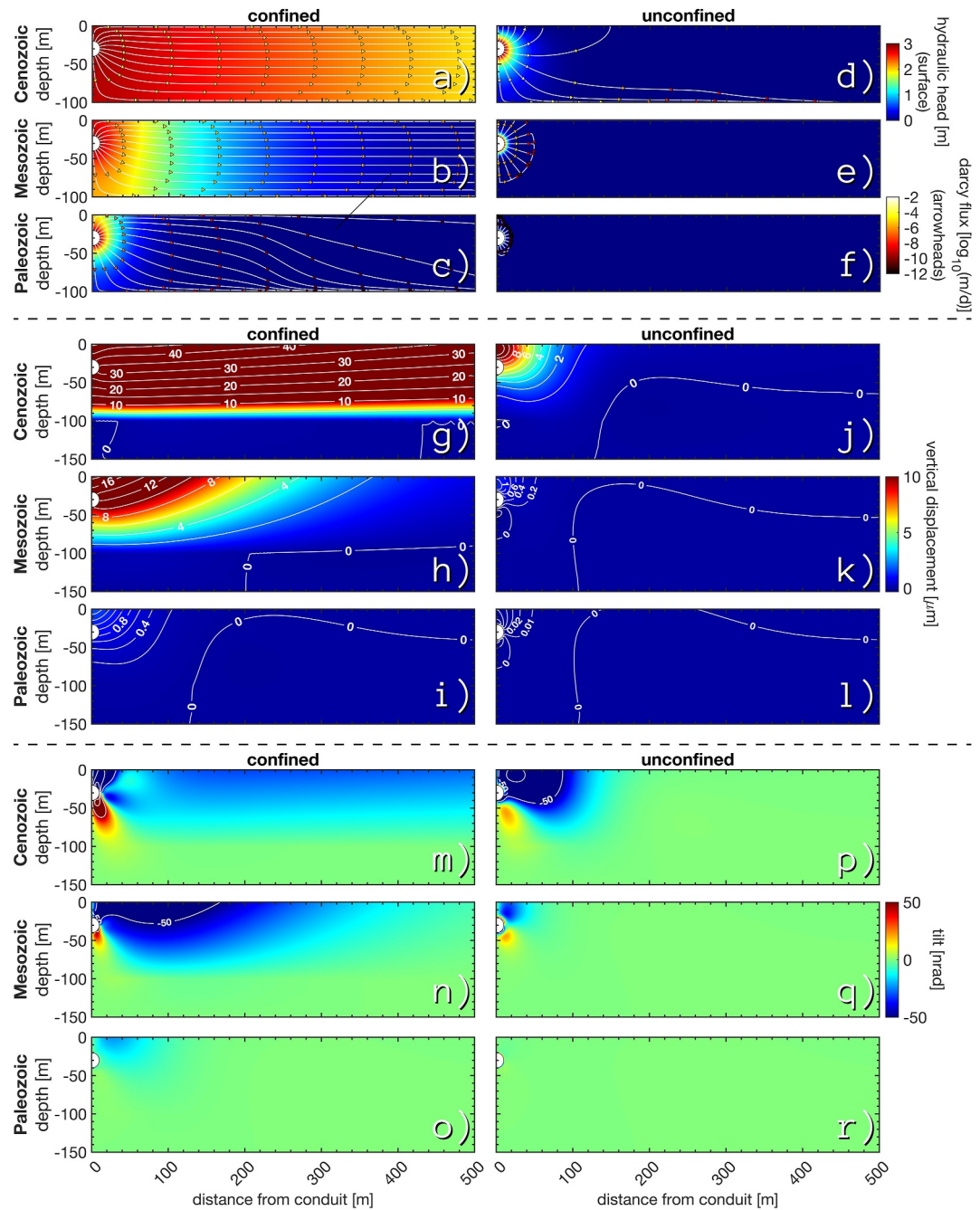


**Figure 2.** Solutions for aquifer cases at  $t = 25$  days. (a–f) Hydraulic head surface and overlaid streamlines with colored arrowheads indicating log-magnitude and direction of Darcy flow field. (g–l) Total vertical displacement with truncated color scale at  $10.0 \mu\text{m}$ . Contours specific to each case are added. (m–r) Tilt with truncated color scale at  $\pm 50$  nrad. Contours are added from  $\pm 50$  to  $\pm 250$  nrad in  $100$  nrad intervals. Depths  $> 100$  m corresponds to the lower-confining unit. Confined and unconfined cases are presented in the left and right columns, respectively. Paleozoic, Mesozoic, and Cenozoic aquifers are presented in the different rows (see labels).

## 4. Results

### 4.1. Solutions Over the Full Model Domain

Hydraulic head and Darcy flux magnitude are spatially distributed further from the conduit for the confined versus unconfined cases of a given rock age (Figures 2a–2f). For the confined and unconfined cases, the spatial

distribution of the hydraulic head and Darcy flux magnitude increases with decreasing rock age. For all cases, fluid flows radially outward from the conduit where maximum changes in hydraulic head and Darcy flux occur. Flow does not become “truly” horizontal for all cases except for the Mesozoic and Cenozoic confined cases. Instead, fluid flow for the Paleozoic and Mesozoic unconfined cases stays in the vicinity radially adjacent to the conduit such that the Darcy flux magnitude rapidly decreases away from the conduit until a discoidal flow pattern occurs (Figures 2e and 2f). For the Paleozoic confined and Cenozoic unconfined cases, the spatial distribution of hydraulic head is similar, but the behavior of the streamlines is different (Figures 2c and 2d). In the Paleozoic confined case, flow initially moves toward and follows the upper and lower boundaries near the conduit but diminishes at around 200 m from the conduit, where it tends to flow downward toward the bottom of the aquifer. In the Cenozoic unconfined case, however, flow from the upper half of the conduit predominantly moves vertically and truncates at the upper boundary. In contrast, flow from the lower half descends and follows the lower confining unit. The Darcy flux is several orders of magnitude greater at similar spatial coordinates for the Cenozoic unconfined case versus the Paleozoic confined case. For the Mesozoic and Cenozoic confined cases, the flow becomes horizontal at approximately 150 m from the conduit (Figures 2a and 2b).

Maximum total vertical displacement occurs in the local vicinity above the conduit and decreases with distance from the conduit (Figures 2g–2l). Vertical displacement extends to distances further from the conduit for the confined versus unconfined cases of a given rock age. Similarly, for both confined and unconfined cases, vertical displacement subsequently spans further from the conduit with decreasing rock age. There is approximately a one order of magnitude decrease in the vertical displacement between the confined and unconfined cases for similar rock age as well as vertical displacement increases with decreasing rock age for each aquifer type. The spatial distribution of the vertical displacement is similar for the Paleozoic confined and the Cenozoic unconfined aquifer cases, but vertical displacement for the Cenozoic unconfined case is approximately one order of magnitude larger (Figures 2i and 2j).

The modeled tilt patterns exhibit a dominant spatial orientation, pointing away from the conduit (Figures 2m–2r). This negative (clockwise) tilt originates near the upper-right quadrant of the conduit, whereas localized positive (counterclockwise) tilt signal is present near the lower-right quadrant. Because the model is symmetrical (mirrored) along the  $x = 0$  plane, polarity of the tilt is reversed for negative  $x$ -distances. Among the studied cases, the Paleozoic cases show the least absolute tilt magnitude (Figures 2o and 2r). Specifically, the Paleozoic unconfined case exhibits little-to-no tilt signal away from the conduit-matrix boundary, whereas the Paleozoic confined case displays its greatest absolute tilt magnitude near the upper boundary ( $\ll 50$  nrad). On the other hand, the Paleozoic and Mesozoic unconfined cases demonstrate localized absolute maximum tilt at the conduit-matrix boundary (Figures 2q–2r). In contrast, the Cenozoic cases exhibit the highest absolute tilt magnitude among all model cases (Figures 2m and 2p). In the Cenozoic confined case, this occurs at the conduit-matrix boundary ( $\gg 250$  nrad) (Figure 2m), whereas in the Cenozoic unconfined case, it is observed near the upper boundary (150–250 nrad) (Figure 2p). For the Mesozoic and Cenozoic confined cases, the absolute maximum tilt occurs at the conduit-matrix boundary (Figures 2m and 2n). Moreover, the overall negative tilt of the Mesozoic confined case more locally restricted to the conduit than the Cenozoic confined case. However, the Mesozoic confined case exhibits a larger spatial distribution of absolute tilt exceeding 50 nrad, whereas in the Cenozoic confined case, tilt magnitudes greater than 50 nrad are concentrated closer to the conduit. This is explained by the small gradient of vertical displacement for the confined Cenozoic case (Figure 2g). Additionally, the Cenozoic confined case shows a distinct local minimum at distances of 40–50 m from the conduit in the upper-half of the model permeable zone.

#### 4.2. Solutions at Fixed Positions

The hydraulic head solutions are compared at  $y = -30$  m (Figures 3a and 3b). The solutions are greatest at the conduit-matrix boundary and degrade with distance from the conduit. The signals for the confined and unconfined cases extend approximately 0.1, 0.6, and 4.0 km and 15, 25, and 100 m from the conduit center ( $x = 0$ ), respectively, with decreasing rock age.

At the upper boundary, the total vertical displacement signals in the confined cases extend approximately the same distance from the conduit as the hydraulic head signals, while they extend up to 50 m further than the hydraulic head signals in the Mesozoic and Cenozoic unconfined cases (Figures 3c and 3d). The confined cases exhibit subsequently increasing vertical displacement with decreasing rock age, that is, with increasing Biot coefficients and compliances (up to 48  $\mu\text{m}$  difference at  $x = 0$ ) (Figure 3c). This trend holds for the unconfined

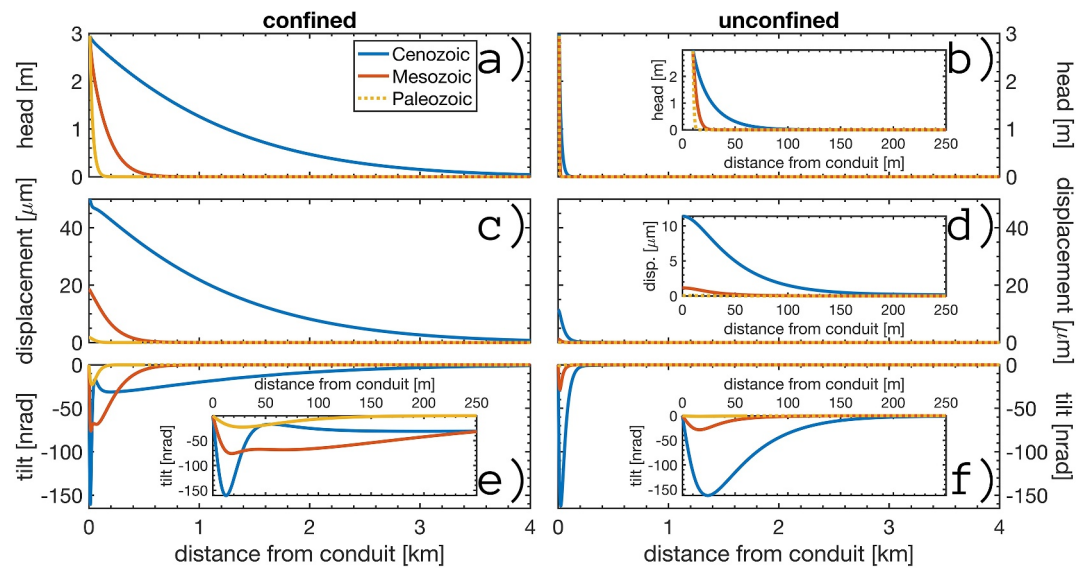


**Figure 3.** Solutions of (a), (b) hydraulic head at  $y = -30$  m, (c), (d) vertical displacement, and (e), (f) tilt at the upper boundary for  $x \leq 4$  km and  $t = 25$  days for different limestone ages (Table 2). Confined and unconfined cases are presented in the left and right panels, respectively. Inset graphs for distances  $x \leq 250$  m are included for selected solutions and indicated by the gray dashed boxes.

cases, but some signals are insignificant. For instance, there is no significant response for the Paleozoic unconfined case, the Mesozoic unconfined case exhibits only small vertical displacement ( $< 2 \mu\text{m}$ ), and the Cenozoic unconfined case has a relatively large response ( $\sim 11 \mu\text{m}$ ) (Figure 3d).

A secondary peak is evident in the vertical displacement for the Cenozoic confined case near the conduit ( $\sim 50$  m) (Figure 3c), and is directly reflected in the tilt as a local minimum (Figure 3e). The Mesozoic confined case exhibits similar behavior and reaches a local minimum about 40 m from the conduit. This behavior, however, is not seen in the Paleozoic confined case, for which the tilt signal resembles the smooth increase and decrease of the Mesozoic and Cenozoic unconfined cases (Figures 3e and 3f). Absolute tilt for confined cases occurs closer to the conduit for younger rock, while absolute tilt for the unconfined cases occurs at larger distances from the conduit for younger rock.

As distance from the conduit increases, both temporal hydraulic head and total vertical displacement solutions show slower increases for each specific scenario (Figures 4a–4p). Furthermore, in confined cases compared to unconfined cases of the same rock age, these increases occur more rapidly. These increases are less linear for Paleozoic and Mesozoic confined and Cenozoic unconfined cases. There is a larger time delay of the response signal at increasing distance. The Paleozoic confined case takes up to 5 days to respond for distances less than or equal to 70 m from the conduit (Figures 4a–4c and 4i–4k) with no response at 175 m from the conduit (Figures 4d and 4l). The Mesozoic confined case responds quicker than the Paleozoic confined case. This response is almost instantaneous at 15 m from the conduit (Figures 4a and 4i) and less than 5 days for distances between 45 and 175 m from the conduit (Figures 4b–4d and 4j–4l). The Cenozoic confined case has nearly an instantaneous response at all distances up to 175 m from the conduit (Figures 4a–4d and 4i–4l). There is no significant hydraulic head or displacement signal for the Paleozoic and Mesozoic unconfined cases (Figures 4e–4h and 4m–4p). Time delays for the Cenozoic unconfined case resemble the Paleozoic confined case.

In the Paleozoic and Mesozoic confined cases, the tilt exhibits the smallest absolute magnitude directly above the conduit; however, the highest absolute magnitude is observed at distances of 45 and 70 m from the conduit, respectively (Figures 4q–4t). The effects of the local minimum in absolute tilt for the Cenozoic confined case are apparent as a rapid decrease in the slope in the tilt curve at distances greater than 45 m from the conduit (Figures 4r–4t). For the unconfined cases, absolute magnitude tilt of younger rock is always greater than or equal to that of older rock (Figures 4u–4x). The Paleozoic unconfined case exhibits little-to-no tilt. Tilt in the Mesozoic unconfined case is consistently smaller than the Mesozoic confined case. However, at distances between 45 and

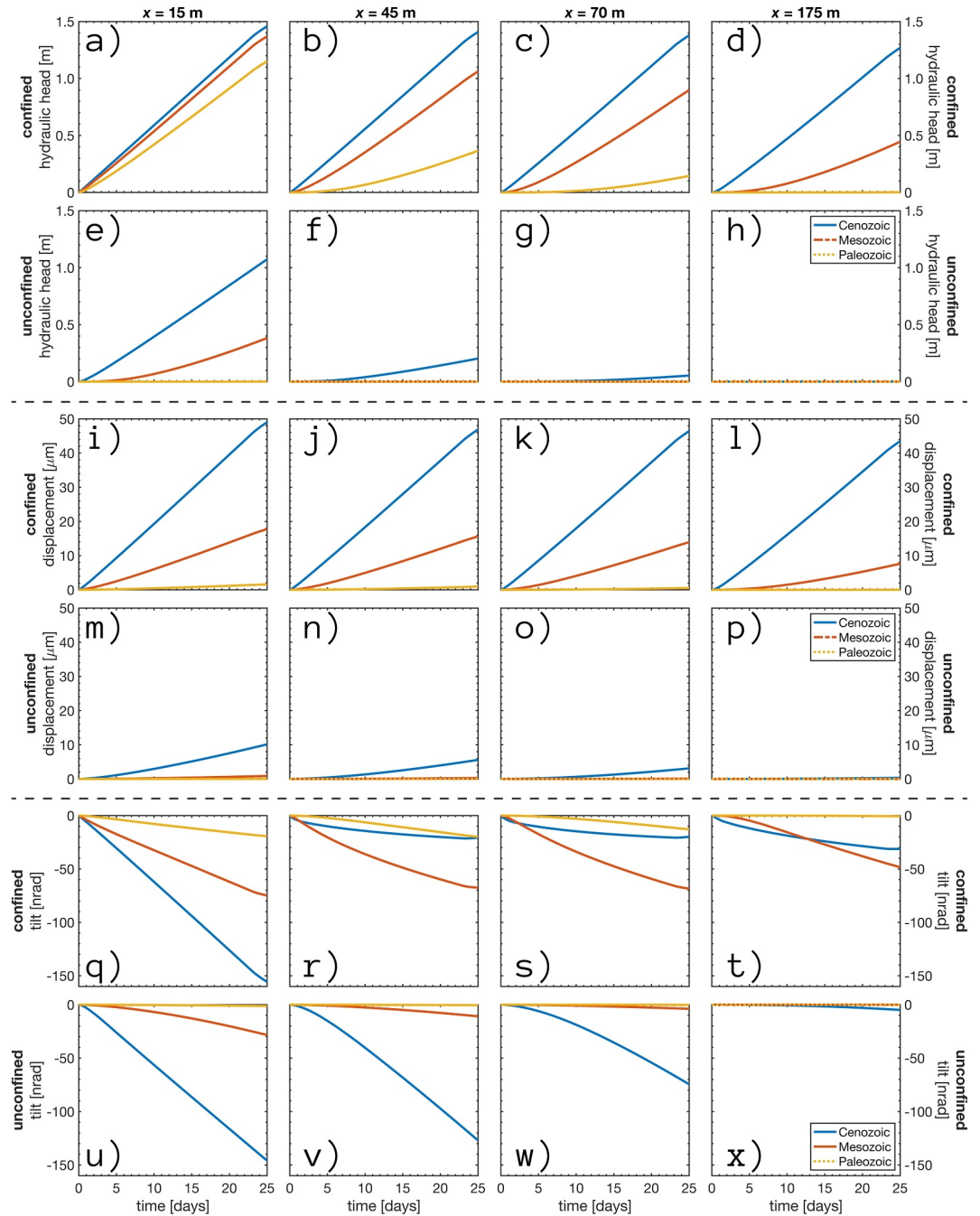


**Figure 4.** Temporal solutions at  $x = 1, 45, 70,$  and  $175$  m for different limestone ages (Table 2) of (a–h) hydraulic head at  $y = -30$  m, (i–p) vertical displacement and (q–x) tilt at the upper boundary. Confined and unconfined cases are included (see lateral labels).

70 m from the conduit, tilt absolute magnitude in the unconfined Cenozoic case is larger than the confined Cenozoic case.

### 4.3. Solutions at the Upper Boundary Considering Varying Conduit Radii and Depth

Conduit radii of 1, 5, 10, and 15 m at a fixed depth of 30 m to the conduit center are considered for Cenozoic confined and unconfined aquifer cases (Figure 5). Increasing the conduit radius appears to predominantly affect the magnitude of the poroelastic response and minimally alter the spatial extent. For the unconfined cases, the

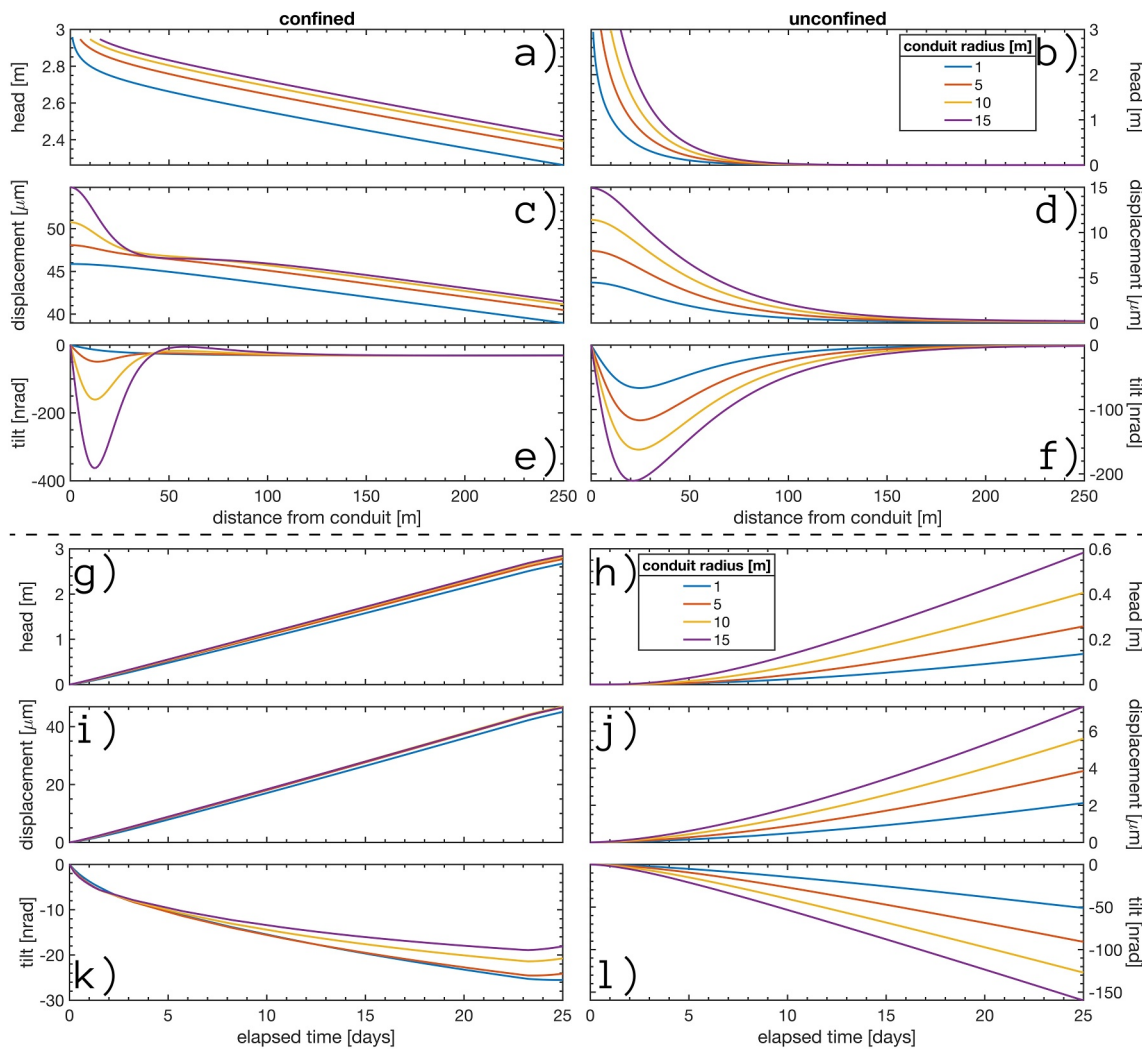


**Figure 5.** Conduit radius case solutions (a–f) at  $t = 25$  days for  $x \leq 250$  m and (g–l) at  $t \leq 25$  days for  $x = 45$  m. Hydraulic head is examined at  $y = -30$  m and vertical displacement and tilt at the upper boundary.

increase in radius produces notable responses across all spatial and temporal solutions (Figures 5b, 5d, 5f, 5h, 5j, and 5l). For example, given a 5 m increase in conduit radius, at  $x = 45$  m and  $t = 25$  days, hydraulic head, vertical displacement, and tilt increase by approximately 0.2 m, 2  $\mu\text{m}$ , and 30–40 nrad, respectively. The confined cases, however, show only a subtle increase in hydraulic head with increasing conduit radius (up to 0.2 m; Figures 5a and 5g). The confined cases show the largest differences in the total vertical displacement directly above the conduit (2–4  $\mu\text{m}$ ), and the secondary peak broadens with increasing conduit radius (Figure 5c). Notably, the 1 m conduit does not appear to produce this behavior. The relatively small changes in vertical displacement manifest in the tilt signals with changes of 100's of nrad locally near the conduit (Figure 5e). Temporally there is little-to-no difference in hydraulic head and vertical displacement at 45 m (Figures 5g and 5i). The rate-of-change of tilt magnitude, however, decreases with time at  $x = 45$  m (Figure 5k). Initially, tilt magnitude is slightly larger for larger conduit radii, but by the end of the simulation, tilt magnitude is smaller for larger conduit radii.

Conduit depths of 15, 30, 45, and 60 m and with a fixed radius of 10 m are considered at fixed positions for Cenozoic confined and unconfined aquifer cases (Figure 6). There is little difference in hydraulic head for the confined cases (Figures 6a and 6g). Conversely, for the unconfined cases, there are relatively large decreases in hydraulic head (up to 1.0 m) with increasing conduit position above and below  $y = -30$  m (Figure 6b). At the upper boundary, the vertical displacement for the confined cases generally decreases with increasing conduit depth (Figure 6c). For instance, the largest differences are directly above the conduit (up to 4  $\mu\text{m}$ ). At  $x = 45$  m, we

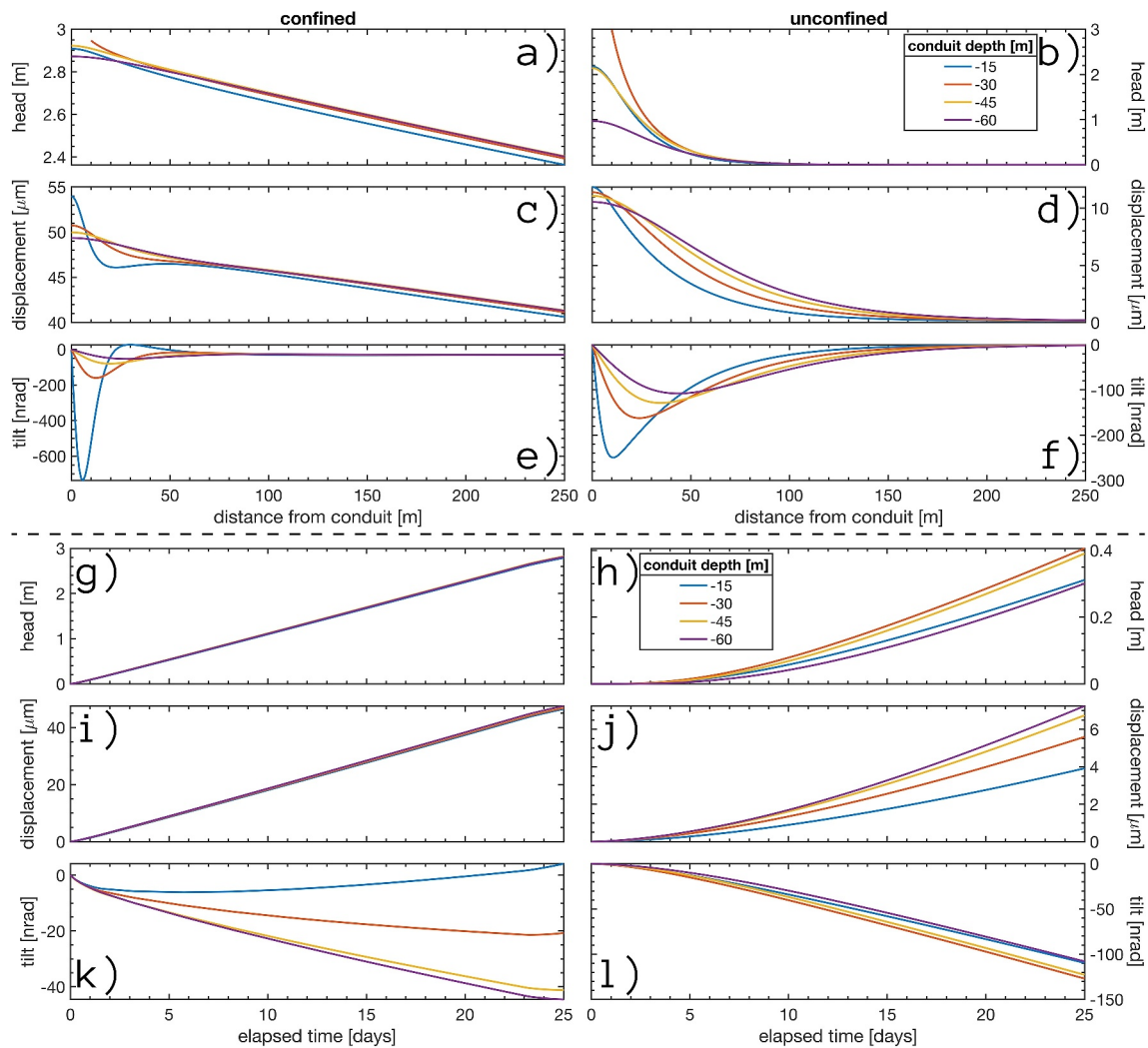


**Figure 6.** Conduit depth case solutions (a–f) at  $t = 25$  days for  $x \leq 250$  m and (g–l) at  $t \leq 25$  days for  $x = 45$  m. Hydraulic head is examined at  $y = -30$  m and vertical displacement and tilt at the upper boundary.

find no difference in vertical displacement (Figure 6i). The secondary peak in the vertical displacement is more pronounced for shallower conduits. Its inflection point in the vertical displacement as well as absolute maximum tilt is located closer to the conduit for shallower conduits. Tilt for all confined cases becomes equal at distances greater than 100 m from the conduit. For the unconfined cases, vertical displacement above the conduit decreases (up to  $\sim 1 \mu\text{m}$ ) with increasing conduit depth (Figure 6d). This leads to smaller tilt magnitude near the conduit (Figure 6f). Away from the origin, vertical displacement decreases more rapidly for shallower conduits. That is, by 50 m from the conduit, the deeper conduits generally lead to larger vertical displacement than the shallower conduits and comparable absolute tilt (Figures 6d, 6f, 6j, and 6l).

## 5. Discussion

### 5.1. Aquifer Cases

Hydraulic diffusivity ranges over seven orders of magnitude across all tested cases (Table 2), which is related to differences in aquifer age (one to two orders of magnitude differences in hydraulic diffusivity) and aquifer type (i.e., confined or unconfined, differences of three to four orders of magnitude in hydraulic diffusivity). As expected, the hydraulic diffusivity governs the spatial distribution of the hydrological response. Hydrologic signals generally propagate much slower in older unconfined aquifers (e.g., Paleozoic) than they do in younger confined

aquifers (e.g., Cenozoic), while a similar response may be expected in older confined and younger unconfined aquifers with a similar hydraulic diffusivity.

Because of the assumption of instantaneous deformation response to pressure changes, the hydraulic diffusivity must also govern the spatial distribution of the deformational response. This is seen in the vertical displacement and subsequent tilt solutions, which have nearly the same spatial distribution as the hydraulic head solutions (Figures 2–4). It may be inferred, however, that the hydraulic diffusivity does not control the magnitude of this response, which is conspicuous given that the vertical displacement for the Paleozoic confined case is approximately one order of magnitude less than the Cenozoic unconfined case (Figures 2i and 2j). Instead, the magnitude of the deformational response is governed by an interaction between the hydraulic diffusivity, Biot-Willis coefficient and the elastic moduli of the aquifer (Table 2). Smaller values of Young's modulus directly lead to increased vertical deformation. Larger values of Poisson's ratio allow the system to be less compressible (Equation 4) and force a two-dimensional deformational response to a one-dimension stress deviation by definition. This means that larger values of Poisson's ratio slightly decrease the deformation predicted just by Young's modulus. Additionally, larger values of the Biot-Willis coefficient allow for increased deformation, which is a consequence of its role in the effective stress obtained by rearranging Equation 1. A larger magnitude in vertical displacement does not imply a larger tilt signal. This is apparent in the solutions for the Cenozoic confined case versus the Mesozoic confined and Cenozoic unconfined cases (Figures 2g–2r and 4i–4x), which suggests that if a given aquifer has a large hydraulic diffusivity and a small Young's modulus, then relatively large displacement may be of long spatial wavelength with a small displacement gradient such that the tilt is relatively small.

The secondary peak seen in the displacement and subsequent local minimum in the tilt solutions for the Mesozoic and Cenozoic confined cases are presumably the result of increased stress above and below the conduit (Figures S9 and S10 in Supporting Information S1). To evaluate if this could lead to rock failure, we compare von Mises stress and maximum principal stress to compressive and tensile strength, respectively (Gudmundsson, 2011; Jaeger et al., 2007). Compressive and tensile strength of limestone range on the order of 4–100 MPa and 1–8 MPa, respectively (Gudmundsson, 2011), which is several orders of magnitude greater than the calculated stress (>10 kPa). Therefore, rock failure is not likely under these circumstances. It is also unlikely that this behavior is resolvable via tilt data without an impractically dense instrument array.

From this modeling exercise, it may be inferred that a rudimentary estimate of aquifer hydraulic diffusivity can guide the expected spatial hydrological and deformational response pattern of the aquifer, which has implications for geophysical array design, well network design, contaminant transport, general water quality and karst development. For areas where conduit location may be constrained, geodetic arrays should be denser and focused closer to the conduit for older rock and unconfined aquifers. Furthermore, the polarity of the tilt signal (Figures 2m–2r and 4q–4x) could potentially provide means to identify relative locations of unknown conduits. Braitenberg et al. (2019) came to a similar conclusion and further suggested that large GPS arrays could also determine conduit location for large systems, but this requires a physical system capable of generating displacements on the order of several millimeters at least.

It may prove difficult to estimate conduit size and in particular depth because the model geometry can lead to non-unique solutions. It can be inferred from the conduit radius and depth cases that the model solutions are more sensitive to conduit size than depth, with the arguable exception of tilt solutions of the confined case (Figures 5 and 6). From this it may be hypothesized that a larger and deeper conduit could produce the same solutions at the upper boundary as a smaller shallower conduit. This was tested by additional simulations, considering only the Cenozoic unconfined case, where conduit depth was successively increased from 6 to 54 m in 8 m increments, and the corresponding conduit radius was determined such that the maximum absolute tilt at the upper boundary are effectively equal to that of the original fixed 10 m radius conduit at 30 m depth. The results indicate that increasing the conduit radius and depth leads to broader vertical displacement signals where maximum tilt occurs further from the conduit (Figure S11 in Supporting Information S1). This results in larger vertical displacement and broader spatial coverage for each successive increase in conduit radius and depth, and approximately a 5 m increase in distance from the conduit where maximum absolute tilt occurs. Also, we find a quadratic relationship between conduit radius and depth (Figure S12 in Supporting Information S1). Therefore, small tilt arrays can provide information on the relative conduit size and depth, given that the model parameters are well constrained, and an iterative deployment of tiltmeters based on prior observations could be used to characterize and monitor conduit-matrix systems.

## 5.2. Data Observations

To test the applicability of the Cenozoic models and compare them with natural data, we adopted a 100 days data set (1 July 2019–9 October 2019). We chose this date range specifically because it contains two notable peaks in the hydrograph, coinciding with when the majority of our hydrological and geophysical equipment were operational. Although we do not have direct measurements of conduit pressure, we inferred the conditions within the conduit from the surface water levels within the karst windows (i.e., sinkholes that generally represent collapsed portions of the conduit) Sweetwater Lake, Paraner's Branch, Jug Lake, Hawg Sink, and Ogden Pond (Figure 1b and Figure S4 in Supporting Information S1). For simplicity, we assumed that karst window water level is representative of conduit pressure head. We used data from Paraner's Branch as the hydraulic head input at the conduit-matrix boundary and compare the results to monitoring wells 3 and 5, approximately 55 and 125 m from the conduit, respectively (Figure 1). These data are down sampled from an original rate of 2 min to 0.25 days and lowpass filtered with a cutoff period of 2 days to eliminate high frequency noise.

The tilt stations RE1T and RE2T were placed in boreholes (6–8 m depth) within the uppermost unconsolidated sand and clay unit and a few meters above bedrock. Station SWWP was a platform tiltmeter shallowly buried and vaulted (0.5–1 m depth). To better represent the conditions of the field site in the model, we included a 2 m thick upper layer and test two end-member cases: high hydraulic diffusivity ( $k = 9.97 \cdot 10^{-10} \text{ m}^2$ ,  $S_y = 0.15$ ) sand and low hydraulic diffusivity ( $k = 9.97 \cdot 10^{-15} \text{ m}^2$ ,  $S_y = 5 \cdot 10^{-5} \text{ m}^2$ ) clay (Fetter, 2001; SWFWMD, 2009). This adjustment to the model geometry was crucial as the initial simulations yielded nrad range tilt magnitudes, while  $\mu\text{rad}$  range tilt signals are observed in the data. Also, we fixed the porosity to 0.36 for both cases (Allen, 1985), used typical Poisson's ratio values for sand (0.45) and clay (0.40) (Gudmundsson, 2011), and calculated the Biot-Willis coefficient as a function of porosity as 0.99 based on empirical equations for unconsolidated sediments (Lee, 2003).

To calibrate the model, the hydraulic head result was manually tuned by adjusting the limestone permeability until the output roughly corresponded to the observed water level in Well 3 and Well 5. We found that the size and depth of the conduit can impact the results (Figures 5 and 6, and Figure S11 in Supporting Information S1); however, for this initial calibration, we decided to fix the radius and depth to the reported values of the largest known passages (10 and  $-30$  m, respectively; Moore et al., 2010; Sreaton et al., 2004).

Finally, we manually tuned the Young's modulus of the upper layer until the modeled tilt reflected the observed tilt at RE1T, SWWP, and RE2T, which are approximately 70, 112, and 175 m from the conduit (Figure 1b). Specifications of the tilt equipment and post-processing can be found in Text S5 and Table S5 in Supporting Information S1. Further processing involved rotating the tilt into radial and transverse components, that is, perpendicular and parallel to the conduit, respectively. Also, the tilt data are bandpass filtered between 2 and 27 days with a 6th order Butterworth filter to mitigate against diurnal and transient noise (e.g., temperature and Earth tides). In late July, RE1T experienced equipment issues resulting in a data gap.

The water level and tilt data observations are not replicated by the model in the case of the highly-permeable sand layer and within a reasonable range of hydraulic diffusivity (Figure S13 in Supporting Information S1). Additionally, a conduit size well beyond and much shallower than the known maximum estimates would be needed to reproduce the data observations in the purely unconfined case. However, if we consider a low-permeability clay layer, we are able to capture the magnitude and general behavior of the water levels observed at the monitoring wells (Figures 7a and 7b).

We find that a permeability of  $2.5 \cdot 10^{-11} \text{ m}^2$  results in a good match to the monitoring well observations (within 15 cm) when considering the clay layer. This value of permeability falls slightly beyond the upper end estimates for UFA limestone from core samples, which themselves may range over many orders of magnitude within a single borehole (Budd & Vacher, 2004; Williams & Kuniansky, 2016). However, core sample permeability estimates do not account for the dual-porosity nature of karst systems (Budd & Vacher, 2004; Williams & Kuniansky, 2016). For instance, transmissivities estimated from aquifer pump tests in unconfined or poorly confined regions of the UFA (Williams & Kuniansky, 2016) and from conduit-monitoring well hydraulic head interactions at the SRS (J. M. Martin et al., 2006) suggest that much higher permeability (up to  $6 \cdot 10^{-9} \text{ m}^2$ ) need to be considered to account for aquifer-averaged effects of the dual-porosity system.

The karst sink-spring systems of Florida are part of hydrologically complex areas, generally near boundaries separating confined and unconfined portions of the UFA (Upchurch et al., 2019; Williams & Kuniansky, 2016).

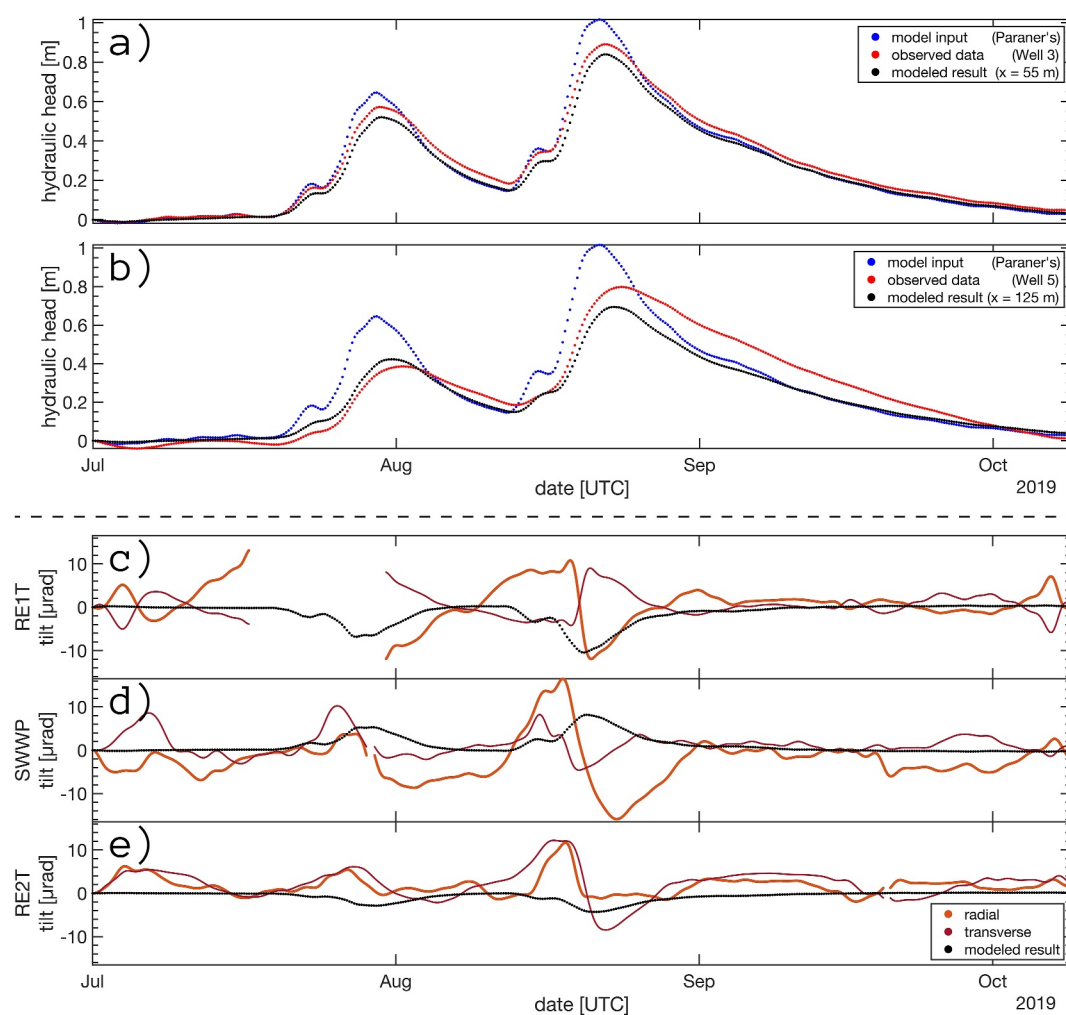


**Figure 7.** (a and b) Observed monitoring well data at (a) Well 3 and (b) Well 5 (red). Modeled hydraulic head results at  $y = -30$  m corresponding to Well 3 ( $x = 55$  m) and Well 5 ( $x = 125$  m) (black) are also displayed, as well as observed karst window water level at Paraner's Branch used as conduit-matrix boundary input (blue). (c)–(e) Observed tilt in the radial (red) and transverse (maroon) components with respect to the conduit direction at (c) RE1T, (d) SWWP, and (e) RE2T. Modeled tilt at the upper boundary corresponding to RE1T ( $x = 70$  m), SWWP ( $x = 112$  m), and RE2T ( $x = 175$  m) (black) are also displayed. All monitoring well and tiltmeter locations are presented in Figure 1.

The confined portions of the UFA are defined by the presence of the clay-rich Hawthorn Group, which are overlain by the same post-Miocene unconsolidated sand and clay unit as the unconfined portions (Miller, 1986). In the confined regions, the overlying unconsolidated unit is referred to as the Surficial Aquifer System (SAS). Sepúlveda and Kuniansky (2011) report that the SAS transitions from highly permeable sand to less permeable silt and clay sands with depth, and the SAS can be partially confined in areas due to the existence of discontinuous clay lenses. From the drill logs of all but one of our tiltmeter boreholes at the SRS, the Florida Geological Survey encountered dense clay between 3 and 6 m depth (D. Paul, personal commun., November 2018). These clay may be acting as a partial confining layer to the limestone unit as suggested by the model results.

We elected to fix the limestone specific yield in the model, but the existence of a partial confining unit could suggest a lower value. Although an actual specific yield eludes us due to the wide-range of possible transmissivity, we can more confidently approximate, from Equation 7, that the aquifer here has a hydraulic diffusivity of approximately  $0.16 \text{ m}^2/\text{s}$ .

Modeled tilt at  $y = 0$  m and at the corresponding station distances from the conduit is also shown in Figures 7c–7e. We find that a clay Young's modulus of 2 MPa produced tilt of the correct order of magnitude, which is consistent

with lower-end estimates of soft clay (Bowles, 1997). The polarity of the modeled tilt depends on which side of the conduit the respective observations are located on and whether the conduit is being pressurized or unpressurized. Stations which are east of the conduits (e.g., RE1T and RE2T) should exhibit dominantly negative tilt in the radial component, while stations west of the conduits (e.g., SWWP) should have dominantly positive tilt in the radial component. Although observed data from both radial and transverse components are plotted, there is zero tilt in the model solution for the transverse component given the 2D nature of the model.

If the assumptions of the model are entirely correct, and the tilt records do not include unmodeled effects, then signals should be observed only in the radial component. Stations RE1T and SWWP show dominant tilt in the radial component, and both appear to have captured the modeled peaks (Figures 7c–7e). Observations at both locations generally have the same polarity, although SWWP exhibits a polarity reversal during the second peak in late August. Station RE2T, however, expresses a dominant signal in the transverse component and also experiences a polarity reversal (Figure 7e). The signals in the transverse components of RE1T and SWWP and radial component of RE2T are lower in magnitude and noisier than in the other component.

Reversals in polarity and signal present in both components suggest multiple source locations. This is because a single conduit would produce an observable signal only in the radial component with polarity consistent to that of the model prediction, otherwise there must be additional source locations, apparently activated in phase with the modeled source. Polarity reversals further suggest that the dominant signal source location may not be temporally constant. Because the reversals occur during the second larger peak in late August, this could be indicative of flow path changes, such as activation of overflow paths or direct loading due to increased karst window water levels. Also, the signals could be affected by additional noise sources such as temperature variations or Earth tides not fully filtered out by the data post processing.

The results suggest that additional heterogeneities need to be carefully considered to improve this model. The first order dynamics of the tilt observations are, however, adequately captured, as observed tilt magnitudes are highest during the times predicted by the model. Future model considerations may include, but are not limited to, a 3D model geometry, additional conduits, and zones of increased permeability and storage (e.g., karst hyporheic zone).

### 5.3. Additional Complexities

In this section, we discuss the main limitations associated with this model and the adopted simplifications.

This study examines the general effects of conduit size, but conduit shape, multiple conduits, and fractures introduce further complications. Identifying such features would require a dense geodetic array that fully transects them or the use of an iterative or compressive sensing framework. Seismic source location methods, such as back azimuth projections (e.g., Vore et al., 2019) and beamforming (e.g., Winberry et al., 2009), may help to resolve source location issues as well. Consideration of fractures or other preferential flow pathways introduces complications similar to the karst conduits because the governing fluid equations may need to be modified to explicitly consider dual-porosity (e.g., Barenblatt et al., 1960; Hernández et al., 2013; Z. Huang et al., 2011) or large fractures would need to be modeled individually (e.g., K. Huang et al., 2020; Jacob et al., 2010; Lesparre et al., 2017; Longuevergne et al., 2009). Furthermore, additional heterogeneities may exist, such that there may be a so-called “karst hyporheic flow zone” surrounding the local conduit vicinity in which there is more significant porosity and permeability than average due to increased dissolution (Dogwiler & Wicks, 2006; Harrelson, 2017; Wilson & Henry, 2014). For example, Harrelson (2017) reported values within the hyporheic zone up to twice as large as those estimated for Cenozoic limestone in Table 2.

Although conduits account for up to 99% of the flow in karst systems (Worthington et al., 2000), and thus, conduits are the main factor governing the introduction and removal of water from storage, diffuse recharge likely accounts for some of the mismatch between the model and data observations.

### 5.4. Comparative Insights and Implications

This study contributes to the understanding of karst aquifer dynamics by exploring poroelastic responses induced by conduit pressurization. In comparison to previous works involving numerical modeling and geodetic observation in karst systems (e.g., Braitenberg et al., 2019; Jacob et al., 2010; Longuevergne et al., 2009), our approach involves fully coupled poroelastic models used to examine the behavior of endmember aquifers. Notably, our

findings align with the advancements of Schuite et al. (2017) and Murdoch et al. (2021, 2023), showing that geodetic observations in aquifers, as described by fully coupled poroelastic models, are sensitive to the geometrical, mechanical, and hydrological properties. Our study demonstrates the validity of incorporating both poroelastic models and geodetic observation by uniquely addressing localized deformation within karst aquifers induced by conduit pressurization. These findings have implications for advancing the broader understanding of the interactions between discrete heterogeneities and the surrounding aquifer, enhancing our ability to monitor and predict localized aquifer behavior.

## 6. Conclusions

We constructed a poroelastic finite element model with the purpose of gaining a better understanding of ground deformation induced by karst conduit pressurization and subsequent changes in groundwater storage. Case studies were performed over parameter sets indicative of Paleozoic, Mesozoic, and Cenozoic confined and unconfined aquifers. Additionally, we considered the effects of various conduit diameters and depths and roughly calibrated the model to observed hydraulic head and tilt data acquired at the Santa Fe River Sink-Rise system in north-central Florida, US.

Results show the influence of hydraulic diffusivity in the behavior of the poroelastic medium when in the presence of a pressurized conduit. Larger values of hydraulic diffusivity (e.g., Cenozoic confined) lead to faster propagation of the poroelastic signal. The Paleozoic confined and Cenozoic unconfined cases have the same order of magnitude hydraulic diffusivity and mark intermediate behavior between the end-members. We find that the mechanical response is influenced by the elastic moduli of the aquifer and Boit-Willis coefficient, resulting in distinctive behavior that varies depending on the rock age. The younger rocks considered are easier to deform. In fact, the Paleozoic confined case experiences less deformation than the Cenozoic unconfined case even though the poroelastic signal has the same spatial pattern. However, this does not translate into larger tilts at the surface because spatially long-wavelength signals may be of large amplitude but the relatively small gradients yield small (i.e., flat) tilts (e.g., Cenozoic confined vs. unconfined cases). Furthermore, polarity of the tilt signal could be an indicator of relative conduit location, depth, and size.

Incorporation of observed karst window water level as the conduit-matrix pressure head input yields model results in relative agreement with observed groundwater well and tilt data. The model suggests partially confined behavior due to an overlying clay layer. The spatial distribution and magnitude of the hydrologic response is well predicted by the model (within 15 cm). Although the modeled tilt captures the overall trend of the observed data, it fails to predict the observed polarity reversals. The model is also limited by its 2D nature, which allows it to predict only one component of tilt perpendicular to the conduit. In reality, we observe tilt in both perpendicular and parallel components to the known conduit location. These observations suggest that multiple pressurized source locations, not captured by the model geometry, are leading to the tilt observations. Additional geometric and parameter complexities, such as layer thickness, additional layers, and the spatial dependence of the aquifer hydraulic diffusivity, elastic moduli, and/or Biot-Willis coefficient highlight limitations of this simple formulation.

## Data Availability Statement

COMSOL<sup>®</sup> output files, observed hydrological data, observed tilt data, and MATLAB scripts used to create figures are available as part of the Zenodo hydrogeophysics community under <https://doi.org/10.5281/zenodo.8191118> (Gochenour et al., 2023). Observed hydrologic data are also available through HydroShare (Luhmann et al., 2023).

## References

- Allen, J. R. L. (1985). *Principles of physical sedimentology*. Allen and Unwin.
- Anderson, M. P., Woessner, W. W., & Hunt, R. J. (2015). *Applied groundwater modeling: Simulation of flow and advective transport* (2nd ed., p. 533). Elsevier.
- Bailly-Comte, V., Martin, J. B., Jourde, H., Screaton, E. J., Pistre, S., & Langston, A. (2010). Water exchange and pressure transfer between conduits and matrix and their influence on hydrodynamics of two karst aquifers with sinking streams. *Journal of Hydrology*, 386(1–4), 55–66. <https://doi.org/10.1016/j.jhydrol.2010.03.005>
- Barenblatt, G. I., Zheltov, I. P., & Kochina, I. N. (1960). Basic concepts in the theory of seepage of homogeneous liquids in fissured rocks [strata]. *Journal of Applied Mathematics and Mechanics*, 24(5), 1286–1303. [https://doi.org/10.1016/0021-8928\(60\)90107-6](https://doi.org/10.1016/0021-8928(60)90107-6)
- Basha, H. A., & Zoghbi, C. A. (2018). Simplified physically based models for pressurized flow in karst systems. *Water Resources Research*, 54(10), 7198–7215. <https://doi.org/10.1029/2018WR023331>

### Acknowledgments

This material is based upon work supported by the National Science Foundation under Grant (1850667). The tilt instrumentation was partly supported by the Incorporated Research Institutions for Seismology (IRIS) through the PASSCAL Instrument Center at New Mexico Tech. The facilities of the IRIS Consortium are supported by the National Science Foundation's Seismological Facilities for the Advancement of Geoscience (SAGE) Award under Cooperative Support Agreement EAR-1851048. Thanks to Jonathan Martin, Madison Flint, Han Byul Woo, Andrew Oberhelman, Joel (Lucas) Cuevas, Tatiana Summerall, Krista Van Der Velde, Jared Ciarico, Lauren Madsen, Calvin Block, Riccardo Ansalidi, and Alexander Janelle for their help in instrument deployment, maintenance, data collection, and demobilization. Special thanks to the Florida Park Service and personnel at O'Leno and River Rise Preserve State Parks and the IRIS-PASSCAL Instrument Center. Last and certainly not least, thanks to all the field critters, especially the ticks, for not causing us any perpetual physical harm.

- Bear, J. (1972). *Dynamics of fluids in porous media*. American Elsevier Publishing Company, Inc.
- Bear, J. (1979). *Hydraulics of groundwater*. McGraw-Hill.
- Bechtel, T. D., Bosch, F. P., & Gurk, M. (2007). *Methods in karst hydrogeology* (1st ed.). CRC Press.
- Benson, R., Yuhr, L., & Kaufmann, R. (2003). Some considerations for selection and successful application of surface geophysical methods. In *Paper presented at the 3rd International Conference on Geophysics*.
- Biot, M. A. (1941). General theory of three-dimensional consolidation. *Journal of Applied Physics*, *12*(2), 155–164. <https://doi.org/10.1063/1.1712886>
- Biot, M. A. (1962). Mechanics of deformation and acoustic propagation in porous media. *Journal of Applied Physics*, *33*(4), 1482–1498. <https://doi.org/10.1063/1.1728759>
- Biot, M. A., & Willis, D. G. (1957). The elastic coefficients of the theory of consolidation. *Journal of Applied Mechanics*, *24*(24), 594–601. <https://doi.org/10.1115/1.4011606>
- Birk, S., Liedl, R., & Sauter, M. (2006). Karst spring responses examined by process-based modeling. *Ground Water*, *44*(6), 832–836. <https://doi.org/10.1111/j.1745-6584.2006.00175.x>
- Bowles, J. E. (1997). *Foundation analysis and design* (5th ed.). The McGraw-Hill Companies, Inc.
- Braitenberg, C., Pivetta, T., Barbolla, D. F., Gabrovšek, F., Devoti, R., & Nagy, I. (2019). Terrain uplift due to natural hydrologic overpressure in karstic conduits. *Scientific Reports*, *9*(1), 1–10. <https://doi.org/10.1038/s41598-019-38814-1>
- Budd, D. A., & Vacher, H. L. (2004). Matrix permeability of the confined floridan aquifer, Florida, USA. *Hydrogeology Journal*, *12*(5), 531–549. <https://doi.org/10.1007/s10040-004-0341-5>
- Chalikakis, K., Plagnes, V., Guerin, R., Valois, R., & Bosch, F. P. (2011). Contribution of geophysical methods to karst-system exploration: An overview. *Hydrogeology Journal*, *19*(6), 1169–1180. <https://doi.org/10.1007/s10040-011-0746-x>
- Choquette, P. W., & Pray, L. C. (1970). Geologic nomenclature and classification of porosity in sedimentary carbonates. *American Association of Petroleum Geologists Bulletin*, *54*(2), 207–250. <https://doi.org/10.1306/5d25c98b-16c1-11d7-8645000102c1865d>
- COMSOL. (2021). COMSOL Multiphysics®: 2021 Release (version 6.0) [Software]. Retrieved from <https://www.comsol.com/release/6.0>
- Courbon, P., Chabert, C., Bosted, P., & Lindsley, K. (2005). *Atlas of great caves of the world*. Dayton. Cave Books.
- Covington, M. D., Wicks, C. M., & Saar, M. O. (2009). A dimensionless number describing the effects of recharge and geometry on discharge from simple karstic aquifers. *Water Resources Research*, *45*(11). <https://doi.org/10.1029/2009WR008004>
- D'Agostino, N., Silverii, F., Amoroso, O., Convertito, V., Fiorillo, F., Ventafriida, G., & Zollo, A. (2018). Crustal deformation and seismicity modulated by groundwater recharge of karst aquifers. *Geophysical Research Letters*, *45*(22), 12253–12262. <https://doi.org/10.1029/2018GL079794>
- Detournay, E., & Cheng, A. H.-D. (1993). Fundamentals of poroelasticity. In C. Fairhurst (Ed.), *Comprehensive rock engineering: Principles, practice and projects analysis and design method* (Vol. 2, pp. 113–171). Pergamon Press. <https://doi.org/10.1016/B978-0-08-040615-2.50011-3>
- Devoti, R., Riguzzi, F., Cinti, F. R., & Ventura, G. (2018). Long-term strain oscillations related to the hydrological interaction between aquifers in intra-mountain basins: A case study from Apennines chain (Italy). *Earth and Planetary Science Letters*, *501*, 1–12. <https://doi.org/10.1016/j.epsl.2018.08.014>
- Diaz, E., Prasad, M., Mavko, G., & Dvorkin, J. (2003). Effect of glauconite on the elastic properties, porosity, and permeability of reservoir rocks. *The Leading Edge*, *22*(1), 42–45. <https://doi.org/10.1190/1.1542755>
- Dogwiler, T., & Wicks, C. M. (2006). Thermal variations in the hyporheic zone of a karst stream. *International Journal of Speleology*, *35*(2), 59–66. <https://doi.org/10.5038/1827-806x.35.2.1>
- Fabian, M., & Kämpel, H.-J. (2003). Poroelasticity: Observations of anomalous near surface tilt induced by ground water pumping. *Journal of Hydrology*, *281*(3), 187–205. [https://doi.org/10.1016/s0022-1694\(03\)00234-8](https://doi.org/10.1016/s0022-1694(03)00234-8)
- Fabricius, I. L., Røgen, B., & Gommessen, L. (2007). How depositional texture and diagenesis control petrophysical and elastic properties of samples from five North Sea chalk fields. *Petroleum Geoscience*, *13*(1), 81–95. <https://doi.org/10.1144/1354-079306-707>
- Fernández, J., Pepe, A., Poland, M. P., & Sigmundsson, F. (2017). Volcano Geodesy: Recent developments and future challenges. *Journal of Volcanology and Geothermal Research*, *344*, 1–12. <https://doi.org/10.1016/j.jvolgeores.2017.08.006>
- Fetter, C. W. (2001). *Applied hydrogeology* (4th ed.). Prentice Hall, Inc.
- Florea, L. J., & Vacher, H. L. (2006). Springflow hydrographs: Eogenetic vs. telogenetic karst. *Ground Water*, *44*(3), 352–361. <https://doi.org/10.1111/j.1745-6584.2005.00158.x>
- Florida Geological Survey. (1997). Well number: W-13785. Columbia county [Dataset]. Retrieved from <https://geodata.dep.state.fl.us/search>
- Ford, D., & Williams, P. (2007). *Karst hydrogeology and geomorphology*. John Wiley & Sons Ltd. <https://doi.org/10.1002/9781118684986>
- Freeze, R. A., & Cherry, J. A. (1979). In C. Brenn & K. McNeily (Eds.), *Groundwater*. Prentice-Hall, Inc.
- Gambino, S., Falzone, G., Ferro, A., & Laudani, G. (2014). Volcanic processes detected by tiltmeters: A review of experience on Sicilian volcanoes. *Journal of Volcanology and Geothermal Research*, *271*, 43–54. <https://doi.org/10.1016/j.jvolgeores.2013.11.007>
- Geertsma, J. (1956). The effect of fluid pressure decline on volume changes of porous rocks. *Paper presented at the 31st Annual Fall Meeting to the Petroleum Branch of the American Institute of Mining, Metallurgical, and Petroleum Engineers*. <https://doi.org/10.2118/728-G-MS>
- Gochenour, J. A., Rinehart, A. J., Grapenthin, R., Luhmann, A. J., & Bilek, S. L. (2023). Data and figure scripts for “poroelastic response to karst conduit pressurization: A finite element modeling exercise toward the use of tiltmeters in karst aquifer monitoring applications”. -v2. *Zenodo*. <https://doi.org/10.5281/zenodo.8191118>
- Gudmundsson, A. (2011). *Rock fractures in Geological processes*. Cambridge University Press.
- Gunn, J. (2015). Analysis of groundwater pathways by high temporal resolution water temperature logging in the Castleton karst, Derbyshire, England. In B. Andreo, F. Carrasco, J. Durán, P. Jiménez, & J. LaMoreau (Eds.), *Hydrogeological and environmental investigations in karst systems* (pp. 227–235). Springer. [https://doi.org/10.1007/978-3-642-17435-3\\_25](https://doi.org/10.1007/978-3-642-17435-3_25)
- Hadi, F. (2018). *Geomechanical characterizations and correlations to reduce uncertainties of carbonate reservoir analysis* (Doctoral dissertation). Missouri University of Science and Technology. Retrieved from [https://scholarsmine.mst.edu/doctoral\\_dissertations/2674](https://scholarsmine.mst.edu/doctoral_dissertations/2674)
- Harrelson, L. B. (2017). *Implementation of field research for karst hyporheic flow in bedrock streams and phreatic caves* (Masters thesis). New Mexico Institute of Mining and Technology.
- Hernández, D., Núñez-López, M., & Velasco-Hernández, J. X. (2013). Telegraphic double porosity models for head transient behavior in naturally fractured aquifers. *Water Resources Research*, *49*(7), 4399–4408. <https://doi.org/10.1002/wrcr.20347>
- Hisz, D. B., Murdoch, L. C., & Germanovich, L. N. (2013). A portable borehole extensometer and tiltmeter for characterizing aquifers. *Water Resources Research*, *49*(12), 7900–7910. <https://doi.org/10.1002/wrcr.20500>
- Huang, K., Luo, X., & Zheng, Z. (2020). Modeling solute transport in karst fissure dual porosity system and application: A case study in an arsenic contamination site. *PLoS One*, *15*(6), 1–16. <https://doi.org/10.1371/journal.pone.0234998>

- Huang, Z., Yao, J., Li, Y., Wang, C., & Lv, X. (2011). Numerical calculation of equivalent permeability tensor for fractured vuggy porous media based on homogenization theory. *Communications in Computational Physics*, 9(1), 180–204. <https://doi.org/10.4208/cicp.150709.130410a>
- Hubinger, B., Birk, S., & Hergarten, S. (2016). A new equation solver for modeling turbulent flow in coupled matrix-conduit flow models. *Ground Water*, 54(4), 596–602. <https://doi.org/10.1111/gwat.12400>
- Hughes, D. S., & Cooke, C. E. J. (1953). The effect of pressure on the reduction of pore volume of consolidated sandstones. *Geophysics*, 18(2), 271–478. <https://doi.org/10.1190/1.1437873>
- Jacob, T., Chéry, J., Boudin, F., & Bayer, R. (2010). Monitoring deformation from hydrologic processes in a karst aquifer using long-baseline tiltmeters. *Water Resources Research*, 46(9), 1–18. <https://doi.org/10.1029/2009WR008082>
- Jaeger, J. C., Cook, N. G. W., & Zimmerman, R. W. (2007). *Fundamentals of rock mechanics* (4th ed.). Blackwell Publishing Ltd.
- Ji, S., Li, L., Motra, H. B., Wuttke, F., Sun, S., Michibayashi, K., & Salisbury, M. H. (2018). Poisson's ratio and auxetic properties of natural rocks. *Journal of Geophysical Research: Solid Earth*, 123(2), 1161–1185. <https://doi.org/10.1002/2017JB014606>
- Kümpel, H.-J., Grecksch, G., Lehmann, K., Rebscher, D., & Schulze, K. C. (1999). Studies of in situ pore pressure fluctuations at various scales. *Oil and Gas Science and Technology*, 54(6), 679–688. <https://doi.org/10.2516/ogst.1999057>
- Kümpel, H.-J., Varga, P., Lehmann, K., & Mentés, G. (1996). Ground tilt induced by pumping—Preliminary results from the Nagycenk test site, Hungary. *Acta Geodaetica et Geophysica Hungarica*, 31(1–2), 67–78.
- Lee, M. W. (2003). *Elastic properties of overpressured and unconsolidated sediments*. U.S. Geological Survey Bulletin 2214.
- Lesparre, N., Boudin, F., Champollion, C., Chéry, J., Danquigny, C., Seat, H. C., et al. (2017). New insights on fractures deformation from tiltmeter data measured inside the Fontaine de Vauluse karst system. *Geophysical Journal International*, 208(3), 1389–1402. <https://doi.org/10.1093/gji/ggw446>
- Longuevergne, L., Florsch, N., Boudin, F., Oudin, L., & Camerlynck, C. (2009). Tilt and strain deformation induced by hydrologically active natural fractures: Application to the tiltmeters installed in Sainte-Croix-aux-Mines observatory (France). *Geophysical Journal International*, 178(2), 667–677. <https://doi.org/10.1111/j.1365-246X.2009.04197.x>
- Luhmann, A. J., Gochenour, J. A., Lam, E. N., Noble, M. W., Kranendonk, E. A., Bilek, S. L., et al. (2023). Hydrologic and meteorological data from the Santa Fe River Sink-Rise flow system area, Florida, USA—May 2018–May 2021 [Dataset]. *HydroShare*. <http://www.hydroshare.org/resource/c6e776fc0c364da7b7702394fbc44842>
- Martin, J. B., & Dean, R. W. (1999). In *Temperature as a natural tracer of short residence times for groundwater in karst aquifers* (Vol. 5, pp. 236–242). Karst Modeling, Karst Waters Institute Special Publication. Retrieved from <http://www.dtic.mil/cgi-bin/GetTRDoc?AD=ADA369937#page=244>
- Martin, J. B., & Dean, R. W. (2001). Exchange of water between conduits and matrix in the Floridan aquifer. *Chemical Geology*, 179(1–4), 145–165. [https://doi.org/10.1016/S0009-2541\(01\)00320-5](https://doi.org/10.1016/S0009-2541(01)00320-5)
- Martin, J. M., Scream, E. J., & Martin, J. B. (2006). Monitoring well responses to karst conduit head fluctuations: Implications for fluid exchange and matrix transmissivity in the floridan aquifer. *Special Papers - Geological Society of America*, 404(17), 209–217. [https://doi.org/10.1130/2006.2404\(17\)](https://doi.org/10.1130/2006.2404(17))
- Miller, J. A. (1986). In *Hydrogeologic framework of the floridan aquifer system in Florida and in parts of Georgia, Alabama, and South Carolina* (Vol. 1403-B). U.S. Geological Survey Professional Paper.
- Miller, J. A. (1990). *Ground water Atlas of the United States: Alabama, Florida, Georgia, South Carolina*. U.S. Geological Survey Hydrologic Investigations Atlas 730-G, Segment 6.
- Moore, P. J., Martin, J. B., & Scream, E. J. (2009). Geochemical and statistical evidence of recharge, mixing, and controls on spring discharge in an eogenetic karst aquifer. *Journal of Hydrology*, 376(3–4), 443–455. <https://doi.org/10.1016/j.jhydrol.2009.07.052>
- Moore, P. J., Martin, J. B., Scream, E. J., & Neuhoff, P. S. (2010). Conduit enlargement in an eogenetic karst aquifer. *Journal of Hydrology*, 393(3–4), 143–155. <https://doi.org/10.1016/j.jhydrol.2010.08.008>
- Murdoch, L. C., DeWolf, S., Germanovich, L. N., Moysey, S., Hanna, A., Roudini, S., & Moak, R. (2023). Using the shallow strain tensor to characterize deep geologic reservoirs. *Water Resources Research*, 59(2), e2022WR032920. <https://doi.org/10.1029/2022WR032920>
- Murdoch, L. C., Germanovich, L. N., Roudini, S., DeWolf, S. J., Hua, L., & Moak, R. W. (2021). A type-curve approach for evaluating aquifer properties by interpreting shallow strain measured during well tests. *Water Resources Research*, 57(9), e2021WR029613. <https://doi.org/10.1029/2021wr029613>
- Pintori, F., Serpelloni, E., Longuevergne, L., Garcia, A., Faenza, L., D'Alberto, L., et al. (2021). Mechanical Response of shallow crust to groundwater storage variations: Inferences from deformation and seismic observations in the Eastern Southern Alps, Italy. *Journal of Geophysical Research: Solid Earth*, 126(2), 1–22. <https://doi.org/10.1029/2020JB020586>
- Ritorto, M., Scream, E. J., Martin, J. B., & Moore, P. J. (2009). Relative importance and chemical effects of diffuse and focused recharge in an eogenetic karst aquifer: An example from the unconfined upper Floridan aquifer, USA. *Hydrogeology Journal*, 17(7), 1687–1698. <https://doi.org/10.1007/s10040-009-0460-0>
- Schuite, J., Longuevergne, L., Bour, O., Burbey, T. J., Boudin, F., Lavenant, N., & Davy, P. (2017). Understanding the hydromechanical behavior of a fault zone from transient surface tilt and fluid pressure observations at hourly time scales. *Water Resources Research*, 53(12), 10558–10582. <https://doi.org/10.1002/2017WR020588>
- Scream, E. J., Martin, J. B., Ginn, B., & Smith, L. (2004). Conduit properties and karstification in the unconfined Floridan aquifer. *Ground Water*, 42(3), 338–346. <https://doi.org/10.1111/j.1745-6584.2004.tb02682.x>
- Sepúlveda, N., & Kumiansky, E. L. (2011). Effects of model layer simplification using composite hydraulic properties. In L. Elango (Ed.), *Hydraulic conductivity: Issues, determination and applications* (pp. 357–376). InTech.
- Serpelloni, E., Pintori, F., Gualandi, A., Scocimarro, E., Cavaliere, A., Anderlini, L., et al. (2018). Hydrologically induced karst deformation: Insights from GPS measurements in the Adria-Eurasia plate boundary zone. *Journal of Geophysical Research: Solid Earth*, 123(5), 4413–4430. <https://doi.org/10.1002/2017JB015252>
- Sheets, R. A., Hill, M. C., Haitjema, K. M., Provost, A. M., & Masterson, J. P. (2015). Simulation of water-table aquifers using specified saturated thickness. *Ground Water*, 53(1), 151–157. <https://doi.org/10.1111/gwat.12164>
- Silverii, F., D'Agostino, N., Borsa, A. A., Calcaterra, S., Gambino, P., Giuliani, R., & Mattone, M. (2019). Transient crustal deformation from karst aquifers hydrology in the Apennines (Italy). *Earth and Planetary Science Letters*, 506, 23–37. <https://doi.org/10.1016/j.epsl.2018.10.019>
- Silverii, F., D'Agostino, N., Métois, M., Fiorillo, F., & Ventafredda, G. (2016). Transient deformation of karst aquifers due to seasonal and multiyear groundwater variations observed by GPS in southern Apennines (Italy). *Journal of Geophysical Research: Solid Earth*, 121(11), 8315–8337. <https://doi.org/10.1002/2016JB013361>
- Southwest Florida Water Management District (SWFWMD). (2009). *Aquifer characteristics within the southwest Florida water management district Report 99–1* (5th ed.).

- Theis, C. V. (1935). The relation between the lowering of the piezometric surface and the rate and duration of discharge of a well using ground-water storage. *Transactions - American Geophysical Union*, 16(2), 519–524. <https://doi.org/10.1029/TRO16i002p00519>
- Tsai, V. C. (2011). A model for seasonal changes in GPS positions and seismic wave speeds due to thermoelastic and hydrologic variations. *Journal of Geophysical Research*, 116(4), 1–9. <https://doi.org/10.1029/2010JB008156>
- Upchurch, S., Scott, T. M., Alfieri, M. C., Fratesi, B., & Dobecki, T. L. (2019). In J. W. LaMoreaux (Ed.), *The karst systems of Florida*. Springer International Publishing. <https://doi.org/10.1007/978-3-319-69635-5>
- Vacher, H. L., & Mylroie, J. E. (2002). Eogenetic karst from the perspective of an equivalent porous medium. *Carbonates and Evaporites*, 17(2), 182–196. <https://doi.org/10.1007/BF03176484>
- Veress, M. (2020). Karst types and their karstification. *Journal of Earth Sciences*, 31(3), 621–634. <https://doi.org/10.1007/s12583-020-1306-x>
- Vesper, D. J., Loop, C. M., & White, W. B. (2000). Contaminant transport in karst aquifers. *Theoretical and Applied Karstology*, 13, 63–73.
- Vore, M. E., Bartholomaeus, T. C., Winberry, J. P., Walter, J. I., & Amundson, J. M. (2019). Seismic tremor reveals spatial organization and temporal changes of subglacial water system. *Journal of Geophysical Research: Earth Surface*, 124(2), 427–446. <https://doi.org/10.1029/2018JF004819>
- Wang, H. F. (2000). *Theory of linear poroelasticity with applications to geomechanics and hydrogeology*. Princeton University Press. <https://doi.org/10.1515/9781400885688>
- Weast, R. C., Astle, M. J., & Beyer, W. H. (1992). In *CRC handbook of chemistry and physics* (67th ed., Vol. 268). 2860(92)85083-s.
- Weise, A., Jentzsch, G., Kiviniemi, A., & Käärjäinen, J. (1999). Comparison of long-period tilt measurements: Results from the two clinometric stations Metsähovi and Lohja, Finland. *Journal of Geodynamics*, 27(2), 237–257. [https://doi.org/10.1016/S0264-3707\(97\)00067-7](https://doi.org/10.1016/S0264-3707(97)00067-7)
- White, W. B. (2002). Karst hydrology: Recent developments and open questions. *Engineering Geology*, 65(2–3), 85–105. [https://doi.org/10.1016/S0013-7952\(02\)00078-6](https://doi.org/10.1016/S0013-7952(02)00078-6)
- Williams, L. J., & Kuniatsky, E. L. (2016). In *Revised hydrogeologic framework of the Floridan aquifer system in Florida and Parts of Georgia, Alabama, and South Carolina* (Vol. 2475, p. 47). U.S. Geological Survey Professional Paper. <https://doi.org/10.3133/pp1807>
- Wilson, J. L., & Henry, K. M. (2014). Computational fluid dynamics modeling of karst conduit-matrix exchanges with relevance to contaminant transport and chemical reactions. *WRR Technical Completion Report No.*, 362, 62.
- Winberry, J. P., Anandkrishnan, S., & Alley, R. B. (2009). Seismic observations of transient subglacial water-flow beneath MacAyeal Ice Stream, West Antarctica. *Geophysical Research Letters*, 36(11), 1–5. <https://doi.org/10.1029/2009GL037730>
- Worthington, S. R. H., Ford, D., & Beddows, P. A. (2000). Porosity and permeability enhancement in unconfined carbonate aquifers as a result of solution. In A. Klimchouk, D. Ford, A. Palmer, & W. Dreybrodt (Eds.), *Speleogenesis: Evolution of karst aquifers* (pp. 463–471). [https://doi.org/10.1016/S0022-1694\(00\)00341-3](https://doi.org/10.1016/S0022-1694(00)00341-3)
- Zhang, S., Zhang, B., Ye, F., & Fu, W. (2022). A closed-form solution for free- and seepage-flow field in axisymmetric infilled conduit. *Ground Water*, 60(1), 112–124. <https://doi.org/10.1111/gwat.13126>

## References From the Supporting Information

- Sethi, R., & Molfetta, A. D. (2019). Groundwater engineering—A technical approach to hydrogeology, contaminant transport and groundwater remediation. In G. Solari, S.-H. Chen, M. di Prisco, & I. Vayas (Eds.), *Springer Tracts in Civil Engineering Series*. Springer. <https://doi.org/10.1007/978-3-030-20516-4>